

# State space geometry of the chaotic pilot-wave hydrodynamics

Nazmi Burak Budanur<sup>1</sup> and Marc Fleury<sup>2</sup>

<sup>1</sup>*Nonlinear Dynamics and Turbulence Group, IST Austria, 3400 Klosterneuburg, Austria<sup>a)</sup>*

<sup>2</sup>*3344 Peachtree Rd, Atlanta, GA 30326*

(Dated: 13 March 2022)

We consider the motion of a droplet bouncing on a vibrating bath of the same fluid in the presence of a central potential. We formulate a rotation symmetry-reduced description of this system, which allows for the straightforward application of dynamical systems theory tools. As an illustration of the utility of the symmetry reduction, we apply it to a model of the pilot-wave system with a central harmonic force. We begin our analysis by identifying local bifurcations and the onset of chaos. We then describe the emergence of chaotic regions and their merging bifurcations, which lead to the formation of a global attractor. In this final regime, the droplet’s angular momentum spontaneously changes its sign as observed in the experiments of Perrard *et al.* (*Phys. Rev. Lett.*, 113(10):104101, 2014).

Keywords: hydrodynamic quantum analogs, symmetry reduction

**During the quantum physics’ infancy, Louis de Broglie<sup>1</sup> imagined it as the outcome of the dynamics of a point-like particle that is interacting with a continuous background field. This viewpoint was to a large extent forgotten during the second half of the twentieth century due to the great success of the Copenhagen interpretation. In recent years, a resurgent interest in de Broglie’s “wave-particle duality” has developed as a result of its discovery in a completely different field: fluid mechanics. In a series of experiments pioneered by Couder *et al.*<sup>2,3</sup>, several phenomena that were once thought to be exclusive to quantum physics were demonstrated in the macroscopic setting of a droplet of silicon oil bouncing on vertically vibrating bath of the same fluid. We examine a class of these systems with rotational symmetry and formulate a novel method for their analysis. We demonstrate the utility of our approach in a numerical study where we describe the chaotic dynamics of a hydrodynamic pilot-wave model through a geometrical approach, in which we identify solutions with qualitative differences and intermittent transitions in between.**

## I. INTRODUCTION

In 2005, Couder *et al.*<sup>2</sup> showed that a droplet of silicon oil can indefinitely bounce on the bath of the same fluid when the bath is vibrating vertically with an acceleration close to but below the Faraday instability point, at which surface waves appear spontaneously. In the same year, Couder *et al.*<sup>3</sup> also reported that a transition from “bouncing” to “walking” takes place when the bath’s oscillation amplitude is large enough. In this latter state,

the droplet becomes a “walker”, and the system exhibits a macroscopic “wave-particle duality”: The force that the droplet experiences at each bounce is determined by the shape of the bath’s surface, which itself is determined by the waves generated at the droplet’s previous bounces. A year later, Couder and Fort reported<sup>4</sup> that when these walkers were realized in single- or double-slit geometries, their final positions obeyed a statistical distribution akin to the single-particle diffraction experiments of quantum particles<sup>1</sup>.

Early experiments with bouncing droplets were followed by others that demonstrated various analogies to the quantum mechanics<sup>7</sup>. Fort *et al.*<sup>8</sup> and Harris and Bush<sup>9</sup> studied walkers in rotating frames and reported quantization of droplet trajectories. Similarly quantized orbits were also found<sup>10</sup> when the two-dimensional pilot-wave system was realized with a central harmonic potential, which was generated by applying magnetic field on a droplet filled with a ferromagnetic fluid. Furthermore, the dynamics of bouncing droplets under central harmonic force was shown to become chaotic<sup>11</sup>. These systems are of particular interest to us due to their rotation symmetry: Assuming the bath’s walls are of circular shape (or far away), governing laws of motion preserve their shape under the rotation of coordinates. As we shall illustrate in this paper, the rotation symmetry translates to a redundant degree of freedom in the system’s state space.

Experimental developments in bouncing droplets were accompanied by modeling efforts. Couder *et al.*<sup>3</sup> already predicted the transition from bouncing to walking as a pitchfork bifurcation by postulating a sinusoidal force to be exerted on the droplet by the bath during the bounces. Through a detailed analysis, Oza *et al.*<sup>12</sup> reached an

<sup>a)</sup>Electronic mail: burak.budanur@ist.ac.at

<sup>1</sup> The single- and double-slit experiments with walkers were revisited by Andersen *et al.*<sup>5</sup> and Pucci *et al.*<sup>6</sup> and the outcomes of these experiments appear to be very sensitive to the experimental conditions.

integro-differential equation of motion for the bouncing droplets and coined the term “pilot-wave hydrodynamics”. Numerical investigations of this model with confining central-potential terms (Coriolis, harmonic, or Coulomb type) demonstrated different routes to chaos<sup>13</sup> and rich subsequent dynamics. Similar to their experimental counterparts, these systems also exhibit rotation symmetry and are at the focus of the current paper.

The references that we cited so far are the key developments in the pilot-wave hydrodynamics literature which are relevant to our work. For a thorough review, we refer the reader to the recent article by Bush<sup>7</sup>. We are now going to turn our attention to a different branch of literature, where chaotic dynamics take place in the presence of continuous symmetries.

In recent years, numerical studies of nonlinear partial differential equations such as the complex Ginzburg–Landau equation<sup>14</sup>, the Kuramoto–Sivashinsky equation<sup>15,16</sup>, and the Navier–Stokes equations<sup>17,18</sup>, demonstrated that degeneracies due to the continuous symmetries in these systems tend to obscure their dynamics. Take, for example, the fluid flow through a cylindrical pipe. This system is symmetric under axial translations and azimuthal rotations. Each generic (non-symmetric) solution of pipe flow has infinitely many copies that can be obtained by continuous symmetry transformations, all of which correspond to the same physical solution. Budanur *et al.*<sup>19</sup> showed that a simple polar-coordinate transformation in the Fourier space representation of these systems can be used to eliminate these redundant degrees of freedom and such a transformation can be interpreted as a “slice”, that is a codimension-1 hyperplane in the state space of the system. This reformulation allowed for the straightforward use of the established geometrical methods of the slicing literature, which were mostly developed within the equivariant bifurcation theory<sup>20</sup>. Budanur *et al.*<sup>19</sup> named this method “first Fourier mode slice” and applied it to the Kuramoto–Sivashinsky equation. Later on, this method was successfully adapted for the simulations of two-dimensional Kolmogorov flow<sup>21</sup> and three-dimensional pipe flow<sup>22,23</sup>. In this paper, we formulate this method for pilot-wave systems and demonstrate its utility in a numerical study.

The rest of this paper is organized as follows. In the next section, we formulate a symmetry-reduced representation of the pilot-wave hydrodynamics with rotation symmetry. At this stage, our treatment will be general and applicable to both experimental and numerical data. In section III, we describe the trajectory equation of Oza *et al.*<sup>12</sup> with an additional central harmonic potential and apply our symmetry-reduction scheme to this system. We analyze the system’s local bifurcations, the transition to chaos via period doubling cascades, and global bifurcations of the system’s chaotic sets. We discuss our results in section IV.

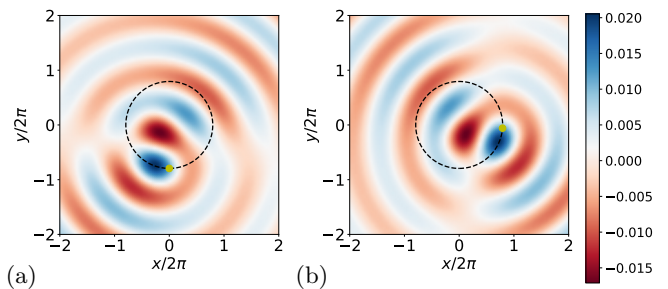


FIG. 1. Two snapshots of a simulated circular trajectory where the trace of the droplet is drawn as a dashed circle and its instantaneous position at the respective snapshot is indicated with a yellow dot in each figure. The magnitude of the wave field color coded in each snapshot. (a)  $\tau = 0$ , (b)  $\tau = 20$  in nondimensional units as explained in section III.

## II. PILOT-WAVE HYDRODYNAMICS AS AN INFINITE-DIMENSIONAL DYNAMICAL SYSTEM

We are going to investigate the dynamics of a point-like droplet as it bounces on the vertically vibrating bath of the same fluid in the presence of a central force. Let us denote the two-dimensional position and velocity of the droplet at time  $\tau$  with  $\mathbf{r}(\tau) = (x(\tau), y(\tau))$  and  $\mathbf{v}(\tau) = (v_x(\tau), v_y(\tau))$  respectively, and the fluid height on the bath surface as a function of polar coordinates  $r$  and  $\theta$  at time  $\tau$  with  $h(r, \theta; \tau)$ . We assume that the future time-evolution of the system is completely determined by the current position and velocity of the droplet and the shape of the bath’s surface. Under this assumption, we can define a state space vector

$$a(\tau) = (\mathbf{r}(\tau), \mathbf{v}(\tau), h(r, \theta; \tau)) \quad (1)$$

and a finite-time flow mapping  $f^\tau(a)$ , which maps an initial state  $a(0)$  to a final state  $a(\tau)$  as

$$a(\tau) = f^\tau(a(0)). \quad (2)$$

Definitions (1) and (2) make up an infinite-dimensional dynamical system since  $h(r, \theta; \tau)$  takes values in a function space. In numerical applications,  $h(r, \theta; \tau)$  would be expressed as a finite-dimensional approximation such as a discretization on a grid, or a spectral expansion. In order to illustrate what we mean by these definitions, we show two snapshots of a simulated (details will be presented in section III) circular trajectory of the pilot-wave system with harmonic potential in figure 1. Snapshots in this figure are separated by 20 nondimensional units of time; and each panel contains the instantaneous information necessary to determine the future evolution of the system. According to our definitions, panel (a) ( $a(0)$ ) is mapped to panel (b) ( $a(20)$ ) by the flow as  $a(20) = f^{20}(a(0))$ .

If we further assume that the flow (2) is smooth, then we can also define the state space velocity

$$\dot{a} = v(a) = \lim_{h \rightarrow 0} (f^h(a) - a) / h \quad (3)$$

and represent the system as an infinite set of ordinary differential (ODE) equations. In general, especially for experimental data, it may not be possible to obtain an explicit ODE form (3). Nevertheless, if the dynamics is sufficiently smooth, we can assume that the state space velocity  $v(a)$  (3) exists and we are going to use its definition (3) in what follows.

### II.1. The rotation symmetry and the relative invariant solutions

While we have not specified the exact physics that governs the motion of a bouncing droplet yet, the conditions that we described in the previous section along with the additional assumption that the boundaries are far away (or circular) imply rotation symmetry. Since the shape of the bath's surface is determined by the past trajectory and the forcing is only radially dependent; the physics of the problem stays the same under the rotation of coordinates. This, however, does not imply that the solutions would be symmetric under rotations. In fact, it is already visible on the example of figure 1 that the individual snapshots of the circular trajectory do not have rotation symmetry. However, for each generic solution of the system, there exist infinitely many physically equivalent copies that can be obtained by continuous rotations. In the dynamical systems theory, this is called “equivariance”, which we will now formalize for the pilot-wave system.

Let  $g(\phi)$  be the rotation operator which acts on a state vector (1) as

$$\begin{aligned} a' &= g(\phi)a, \\ &= (R(\phi)\mathbf{r}(t), R(\phi)\mathbf{v}(t), h(r, \theta - \phi; t)), \end{aligned} \quad (4)$$

where  $R(\phi)$  are the standard  $2 \times 2$  rotation matrices

$$R(\phi) = \begin{pmatrix} \cos \phi & -\sin \phi \\ \sin \phi & \cos \phi \end{pmatrix}. \quad (5)$$

If for every trajectory  $a(t)$  with  $t \in [0, t_f]$  there exists another one  $g(\phi)a(t)$  obtained by the symmetry action, then the finite-time flow (or equivalently the state space velocity, when it exists) commutes with the symmetry action, i.e.

$$f^\tau(g(\phi)a) = g(\phi)f^\tau(a). \quad (6)$$

We are going to refer to (6) as the “equivariance condition”. Note that the equivariance condition does not imply that the flow is “invariant” under the action of the symmetry, but rather, it transforms as does the state space coordinates themselves. In our treatment, we are going to assume that the pilot-wave systems that we consider satisfy the equivariance condition (6) with the rotation operator defined as in (4).

One way of elucidating the state space geometry of chaotic systems is identifying the time-invariant solutions

(equilibria, periodic orbits, invariant tori ...) that are embedded in the system's chaotic set<sup>24</sup>. In systems with continuous symmetry, roles of these solutions are taken over by their higher-dimensional equivalents, which we will refer to as “relative invariant solutions”. Specifically, a “relative equilibrium” is a solution that evolves only in the symmetry direction at a constant phase speed  $c$ . Let  $a_{\text{REQ}}$  be a state space point on a relative equilibrium, then its time-evolution satisfies

$$a_{\text{REQ}} = g(-c\tau)f^\tau(a_{\text{REQ}}). \quad (7)$$

Note that a time-invariant set is formed by all solutions on the relative equilibrium, i.e. the one-dimensional curve  $\{g(c\tau)a_{\text{REQ}} : \tau \in [0, 2\pi/c]\}$ . The second type of relative invariant solutions we are going to consider here are “relative periodic orbits”, which have trajectories that recur at a symmetry-transformed location after a finite period  $T_{\text{RPO}}$ , i.e.

$$a_{\text{RPO}} = g(-\phi_{\text{RPO}})f^{T_{\text{RPO}}}(a_{\text{RPO}}), \quad (8)$$

where  $a_{\text{RPO}}$  is a point on a relative periodic orbit,  $T_{\text{RPO}}$  is its period, and  $\phi_{\text{RPO}}$  is its phase-shift. Similar to the relative equilibrium, all points on a relative periodic orbits, i.e. the 2-torus  $\{g(\phi)f^\tau(a_{\text{RPO}}) : \phi \in [0, 2\pi), \tau \in [0, T_{\text{RPO}}]\}$ , form a time-invariant set. In other words, the relative invariant solutions that appear as a consequence of a single-parameter continuous symmetry correspond to manifolds with dimensions 1 higher than those of their standard counterparts. Notice that the special case  $c = 0$  in (7) corresponds to an equilibrium solution, and similarly  $\phi_{\text{RPO}} = 0$ , in (8) defines a periodic orbit.

It is possible to define the linear stability of relative invariant solutions by defining Jacobians of (7) and (8)<sup>20,24</sup>. However, we are going to skip these definitions here as they will be redundant once we introduce the symmetry reduction in the next section.

### II.2. Continuous symmetry reduction

Symmetry reduction is a state space coordinate transformation  $a \rightarrow \hat{a}$  such that each symmetry-related (physically equivalent) set of states  $\{g(\phi)a^* \mid \phi \in [0, 2\pi)\}$  is represented by a single solution  $\hat{a}^*$  in the symmetry-reduced state space. An obvious choice of such coordinates for the droplet system with the rotation symmetry is the time-dependent polar coordinate transformation that fixes the polar-angle in  $(x, y)$  plane to a certain arbitrary value. This angle, however, is not defined when the droplet is at the origin, and would experience very rapid phase fluctuations if the droplet is close to the origin. Observing that the droplet's horizontal velocity is always non-zero<sup>3</sup>, we define the following operation

$$\hat{a}(\tau) = g(-\hat{\phi}(\tau))a(\tau) \quad (9)$$

where

$$\hat{\phi} = \text{Arg}(v_x(\tau) + iv_y(\tau)). \quad (10)$$

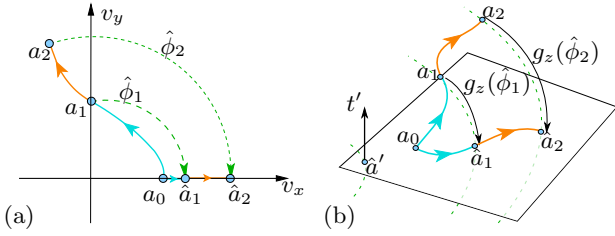


FIG. 2. (a) Schematic illustration of the symmetry reduction as a polar coordinate transformation on the  $(v_x, v_y)$ -plane. (b) Schematic illustration of the symmetry reduction by a slice hyperplane.

This transformation fixes the polar angle in the  $(v_x, v_y)$  plane to 0, hence maps all symmetry-equivalent solutions to the one with  $v_y = 0$  as illustrated in figure 2(a), as long as  $\|\mathbf{v}\| \neq 0$ . Thus, the symmetry-reduced state space coordinates  $\hat{a}$  have  $\hat{v}_y$  coordinate identically equal to 0, i.e.

$$\hat{a} = (\hat{x}, \hat{y}, \hat{v}_x, 0, \hat{h}(r, \theta; t)). \quad (11)$$

Budanur *et al.*<sup>19</sup> showed that a polar coordinate transformation similar to (9), when defined for a partial differential equation with translation symmetry, can be interpreted as a projection onto a codimension-1 hyperplane, named a “slice”, in the state space. We are now going to take analogous steps and redefine the transformation (9) in this terminology in order to exploit the well-established tools of this method.

Let  $\mathcal{T}$  be the generator of infinitesimal rotations satisfying  $g(\phi) = e^{\phi\mathcal{T}}$ . Its action on the state space coordinates can be expressed as

$$\begin{aligned} t(a) &= \mathcal{T}a, \\ &= (T\mathbf{r}(t), T\mathbf{v}(t), (-\partial/\partial\theta)h(r, \theta; t)), \end{aligned} \quad (12)$$

where  $T$  is the generator of the  $2 \times 2$  rotations (5)

$$T = \begin{pmatrix} 0 & -1 \\ 1 & 0 \end{pmatrix} \quad (13)$$

and  $t(a)$  is called the “group tangent” evaluated at  $a$ , since it gives the direction of an infinitesimal rotation at  $a$ . Let us now define the “slice template” as the state vector

$$\hat{a}' = (\hat{x} = 0, \hat{y} = 0, \hat{v}_x = 1, \hat{v}_y = 0, \hat{h}(r, \theta; \tau) = 0), \quad (14)$$

whose only nonzero component is  $\hat{v}_x = 1$ . It is straightforward to verify that the symmetry-reduced state space coordinates (9) satisfy the half-hyperplane condition

$$\langle \hat{a} - \hat{a}', t' \rangle = 0 \quad \text{and} \quad \langle t(\hat{a}), t' \rangle > 0, \quad (15)$$

where  $t' = t(\hat{a}')$  and  $\langle \cdot, \cdot \rangle$  is the inner product defined as

$$\begin{aligned} \langle a_m, a_n \rangle &= x_m x_n + y_m y_n + v_{x,m} v_{x,n} + v_{y,m} v_{y,n} \\ &+ \iint_{\mathcal{D}} w(r) h_m(r, \theta) h_n(r, \theta) r dr d\theta, \end{aligned} \quad (16)$$

where  $w(r)$  is an appropriately chosen weight function and the integral is computed over the whole domain  $\mathcal{D}$ . Projection of the full state space dynamics onto this codimension-1 half-hyperplane is illustrated in figure 2 (b). In the slicing method, one looks for the slice phases  $\hat{\phi}(\tau)$ , such that  $\hat{a}(\tau) = g(-\hat{\phi}(\tau))a(\tau)$  satisfies (15). The main advantage of slicing framework is that it allows for a straightforward symmetry-reduction of the tangent space. Let  $\delta a$  be a small perturbation (in the full state space) to  $\hat{a}$ ; it is projected onto the slice as

$$\delta \hat{a} = H(\hat{a})\delta a, \quad (17)$$

where

$$H(\hat{a}) = \mathbf{I} - \frac{t(\hat{a}) \otimes t'}{\langle t(\hat{a}), t' \rangle}, \quad (18)$$

$\mathbf{I}$  is the identity matrix and  $\otimes$  denotes the outer product. For a derivation, see the appendix of Budanur & Hof (2017)<sup>22</sup>. In particular, we can obtain the symmetry reduced state space velocity  $\dot{\hat{a}} = \hat{v}(\hat{a})$  as

$$\begin{aligned} \hat{v}(\hat{a}) &= H(\hat{a})v(\hat{a}), \\ &= v(\hat{a}) - \frac{\langle v(\hat{a}), t' \rangle}{\langle t(\hat{a}), t' \rangle} t(\hat{a}). \end{aligned} \quad (19)$$

By taking the time derivative of  $\hat{a} = g(-\hat{\phi}(\tau))$  and requiring the slice hyperplane condition (15) to be satisfied, one can show that the multiplier of the group tangent in (19) is in fact the slice phase velocity. In other words, we can write

$$\hat{v}(\hat{a}) = v(\hat{a}) - \dot{\hat{\phi}} t(\hat{a}), \quad (20)$$

$$\dot{\hat{\phi}}(\hat{a}) = \frac{\langle v(\hat{a}), t' \rangle}{\langle t(\hat{a}), t' \rangle}; \quad (21)$$

and integrate the slice phase  $\hat{\phi}$  along with the symmetry-reduced evolution. Rowley and Marsden<sup>25</sup> referred to (20) and (21) as “reconstruction equations” since by integrating them simultaneously, one can reconstruct the full state space evolution. In other words, symmetry reduction does not lose any information, it rather separates the time-evolution into the “physical” (in-slice) and “redundant” (phase) parts. Another observation to make in (21) is that it diverges when  $\langle t(\hat{a}), t' \rangle = 0$ . This, in general, implies that a hyperplane slice that is constructed around an arbitrary template  $\hat{a}'$  is “local”, and applicable in a finite neighborhood where the denominator of (21) is nonzero. Notice, however, that for our particular choice of the slice template (14), this condition becomes  $\langle t(\hat{a}), t' \rangle = \hat{v}_x = \sqrt{v_x^2 + v_y^2}$ ; thus, our slice is applicable as long as the droplet’s velocity does not vanish.

In the symmetry-reduced state space, a relative equilibrium (7) becomes an equilibrium, which satisfies

$$\hat{v}(\hat{a}_{\text{REQ}}) = 0. \quad (22)$$

Linear stability of this solution is determined by the eigenvalue equation

$$\hat{A}(\hat{a}_{\text{REQ}})\hat{e}_i = \lambda_i \hat{e}_i, \quad (23)$$

where  $\hat{A}_{ij}(\hat{a}^*) = \partial \hat{v}_i(\hat{a}) / \partial \hat{a}_j |_{\hat{a}=\hat{a}^*}$ . By straightforward algebra, this matrix is obtained as

$$\hat{A}(\hat{a}) = A(\hat{a}) - \frac{t(\hat{a}) \otimes A(\hat{a})^T t'}{\langle t(\hat{a}), t' \rangle} + \dot{\phi} \frac{t(\hat{a}) \otimes \mathcal{T}^T t'}{\langle t(\hat{a}), t' \rangle} - \dot{\phi} \mathcal{T}, \quad (24)$$

where  $A_{ij}(a^*) = \partial v_i(a) / \partial a_j |_{a=a^*}$ . We are going to refer to  $A(a)$  and  $\hat{A}(\hat{a})$  respectively as the stability matrix and the reduced stability matrix.  $\lambda_i$  are the linear stability eigenvalues and  $\hat{e}_i$  are the corresponding stability eigenvectors within the slice.  $\text{Re } \lambda_i < 0$  and  $\text{Re } \lambda_i > 0$  respectively correspond to the stable and unstable directions associated with the relative equilibrium and a bifurcation takes place when  $\text{Re } \lambda_i = 0$ .

Similar to the relative equilibria, relative periodic orbits (8) satisfy the periodicity condition

$$\hat{a}_{\text{RPO}} = \hat{f}^{T_{\text{RPO}}}(\hat{a}_{\text{RPO}}), \quad (25)$$

where  $\hat{a}(\tau) = \hat{f}^\tau(\hat{a}(0))$  is the symmetry-reduced finite-time flow induced by the dynamics. Consequently, the linear stability of a relative periodic orbit is determined by the eigenvalue equation

$$\hat{J}^{T_{\text{RPO}}}(\hat{a}_{\text{RPO}}) \hat{V}_i = \Lambda_i \hat{V}_i. \quad (26)$$

where  $\hat{J}_{ij}^\tau(\hat{a}^*) = \partial \hat{f}_i^\tau(\hat{a}) / \partial \hat{a}_j |_{\hat{a}=\hat{a}^*}$ . Numerically, the reduced Jacobian  $\hat{J}_{ij}^\tau(\hat{a}^*)$  can be obtained as the time-ordered integral of the reduced stability matrix  $\hat{A}(\hat{a})$  along a symmetry-reduced state space trajectory.  $\Lambda_i$  are known as the Floquet multipliers of the relative periodic orbit and  $\hat{V}_i$  are the corresponding Floquet vectors in the symmetry-reduced state space.  $|\Lambda_i| < 1$  and  $|\Lambda_i| > 1$  correspond to the stable and unstable directions respectively and  $|\Lambda_i| = 1$  corresponds to a marginal direction. Note that the symmetry-reduced state space velocity  $\hat{v}(\hat{a}_{\text{RPO}})$  is an eigenvector of  $\hat{J}^{T_{\text{RPO}}}(\hat{a}_{\text{RPO}})$  with the eigenvalue 1.

This concludes our general introduction of the symmetry-reduction, which can – in principle – be applied to experimental, as well as numerical data, independent of the specifics of system in consideration, as long as the rotation symmetry is present. In the next section, we are going to demonstrate the utility of our transformation by applying it to the simulations of a pilot-wave model with central harmonic force.

### III. A PILOT-WAVE MODEL WITH CENTRAL HARMONIC FORCE

Following the efforts of Moláček and Bush<sup>26</sup>, Oza *et al.*<sup>12</sup> derived a trajectory equation for the bouncing droplets. With the addition of a central harmonic force  $-k\mathbf{r}$ , this equation reads

$$m \ddot{\mathbf{r}} + D \dot{\mathbf{r}} = -mg \nabla h(\mathbf{r}, \tau) - k\mathbf{r}, \quad (27)$$

where  $\mathbf{r} = (x, y)$  is the position of the droplet,  $m$  is its mass,  $D$  is the viscous damping coefficient,  $g$  is the acceleration due to gravity,  $k$  is the effective spring constant

of the harmonic force, and  $h$  is the wave field on the bath surface determined by the previous bounces of the droplet as

$$h(\mathbf{r}, \tau) = A \sum_{n=-\infty}^{\lfloor \tau/T_F \rfloor} J_0(k_F |\mathbf{r} - \mathbf{r}(nT_F)|) e^{-(\tau - nT_F)/T_F Me}, \quad (28)$$

where  $A$  is the initial amplitude of the waves generated,  $J_0$  is the Bessel function of the first kind,  $T_F$  is the time between the bounces, known as the ‘Faraday time’,  $k_F = 2\pi/\lambda_F$  is the wave number corresponding to the least stable Faraday wave, and  $\lambda_F$  is the corresponding wavelength. The tunable parameter  $Me$  is called ‘memory’ and it determines the damping speed of the waves generated in previous bounces. One of the approximations that were made by Oza *et al.*<sup>12</sup> is already apparent from (28), where each bounce instantly generates a Bessel wave, with no time needed for propagation.

With the wave field given as in (28), the trajectory equation (27) is a delay-differential system, which is very hard to study both analytically and numerically. Therefore, Oza *et al.*<sup>12</sup> and several subsequent studies<sup>13,27,28</sup> approximated the sum in (28) by the integral

$$h(\mathbf{r}, \tau) = \frac{A}{T_F} \int_{-\infty}^{\tau} J_0(k_F |\mathbf{r} - \mathbf{r}(\tau')|) e^{-(\tau - \tau')/T_F Me} d\tau'. \quad (29)$$

This approximation is justified since the time scale of the horizontal motion is much greater than the time scale of bouncing<sup>12</sup>. At this stage, (27) is a four-dimensional integro-differential system. Labousse<sup>29,30</sup> showed that this system can further be manipulated into an infinite-dimensional ODEs and this is the form we are going to use in the following. It follows from Graf’s addition theorem<sup>31</sup> that (29) can be written as

$$h(\mathbf{r}, \tau) = A \sum_{n=0}^{\infty} \left[ (2 - \delta_{n,0}) J_n(k_F r) \times (C_n(\tau) \cos(n\theta) + S_n(\tau) \sin(n\theta)) \right] \quad (30)$$

where

$$C_n(\tau) = \int_{-\infty}^{\tau} \frac{d\tau'}{T_F} J_n(k_F r) e^{-(\tau - \tau')/T_F Me} \cos(n\theta(\tau')), \quad (31)$$

$$S_n(\tau) = \int_{-\infty}^{\tau} \frac{d\tau'}{T_F} J_n(k_F r) e^{-(\tau - \tau')/T_F Me} \sin(n\theta(\tau')), \quad (32)$$

We can obtain the time derivatives of the mode amplitudes  $C_n$  and  $S_n$  as

$$\dot{C}_n = -\frac{C_n}{T_F Me} + \frac{1}{T_F} J_n(k_F r) \cos n\theta, \quad (33)$$

$$\dot{S}_n = -\frac{S_n}{T_F Me} + \frac{1}{T_F} J_n(k_F r) \sin n\theta. \quad (34)$$

Rearranging (27), the acceleration of the walker in  $x$  and  $y$  directions can be written explicitly as

$$\ddot{x} = -(D/m) \dot{x} - (k/m) x - g \partial_x h, \quad (35)$$

$$\ddot{y} = -(D/m) \dot{y} - (k/m) y - g \partial_y h, \quad (36)$$

where the partial derivatives are

$$\partial_x h = (\cos \theta \partial_r - r^{-1} \sin \theta \partial_\theta) h, \quad (37)$$

$$= A \sum_{n=0}^{\infty} \left[ (2 - \delta_{n,0}) \times \left( k_F J_{n-1}(k_F r) K_n \cos \theta - \frac{n J_n(k_F r)}{r} L_n \right) \right], \quad (38)$$

$$\partial_y h = (\sin \theta \partial_r + r^{-1} \cos \theta \partial_\theta) h, \quad (39)$$

$$= A \sum_{n=0}^{\infty} \left[ (2 - \delta_{n,0}) \times \left( k_F J_{n-1}(k_F r) K_n \sin \theta + \frac{n J_n(k_F r)}{r} M_n \right) \right]. \quad (40)$$

with  $K_n, L_n$  and  $M_n$  defined as

$$K_n = C_n \cos(n\theta) + S_n \sin(n\theta), \quad (41)$$

$$L_n = C_n \cos[(n+1)\theta] + S_n \sin[(n+1)\theta], \quad (42)$$

$$M_n = S_n \cos[(n+1)\theta] - C_n \sin[(n+1)\theta]. \quad (43)$$

Finally, we nondimensionalize trajectory equations (35) and (36) by scaling time as  $\tau/T_F \rightarrow \tau$  and lengths as  $(k_F x, k_F y) \rightarrow (x, y)$  and rewrite everything compactly as

$$\begin{aligned} \dot{x} &= -\eta \dot{x} - \chi x \\ -\mu \sum_{n=0}^{\infty} (2 - \delta_{n,0}) \left[ J_{n-1}(r) K_n \cos \theta - \frac{n J_n(r)}{r} L_n \right], \end{aligned} \quad (44)$$

$$\begin{aligned} \dot{y} &= -\eta \dot{y} - \chi y \\ -\mu \sum_{n=0}^{\infty} (2 - \delta_{n,0}) \left[ J_{n-1}(r) K_n \sin \theta + \frac{n J_n(r)}{r} M_n \right], \end{aligned} \quad (45)$$

$$\dot{C}_n = -M e^{-1} C_n + J_n(r) \cos(n\theta), \quad (46)$$

$$\dot{S}_n = -M e^{-1} S_n + J_n(r) \sin(n\theta), \quad (47)$$

where,

$$\eta = \frac{DT_F}{m}, \quad \chi = \frac{kT_F^2}{m}, \quad \mu = g A k_F^2 T_F^2. \quad (48)$$

With the addition of trivial equations  $\dot{x} = \dot{x}$  and  $\dot{y} = \dot{y}$ , equations (44–47) yields a set of first order ODEs (3) for the state space vector

$$a = (x, y, \dot{x}, \dot{y}, C_0, C_1, S_1, C_2, S_2, \dots). \quad (49)$$

Formally, this state space is infinite dimensional. In the numerical work to follow, the Fourier-Bessel expansion (30) is truncated at a finite number of  $N+1$  modes (starting counting from the 0th mode), yielding a  $2N+5$  dimensional representation. We define the  $L_2$  inner product in this representation as

$$\langle a_1, a_2 \rangle = \sum_{i=1}^{2N+5} a_{1,i} a_{2,i}. \quad (50)$$

For the state space coordinates ordered as in (49), we can write the rotation-operator (4) explicitly as

$$g(\phi) = \begin{pmatrix} \cos \phi & -\sin \phi & 0 & 0 & 0 & 0 & 0 & \dots \\ \sin \phi & \cos \phi & 0 & 0 & 0 & 0 & 0 & \dots \\ 0 & 0 & \cos \phi & -\sin \phi & 0 & 0 & 0 & \dots \\ 0 & 0 & \sin \phi & \cos \phi & 0 & 0 & 0 & \dots \\ 0 & 0 & 0 & 0 & 1 & 0 & 0 & \dots \\ 0 & 0 & 0 & 0 & 0 & \cos \phi & -\sin \phi & \dots \\ 0 & 0 & 0 & 0 & 0 & \sin \phi & \cos \phi & \dots \\ \vdots & \vdots & \vdots & \vdots & \vdots & \vdots & \vdots & \ddots \end{pmatrix}, \quad (51)$$

with the subsequent  $2 \times 2$  blocks along its diagonal populated with the rotation matrices (5)  $R(2\phi), R(3\phi), \dots$ . The corresponding generator of infinitesimal rotations then becomes

$$\mathcal{T} = \begin{pmatrix} 0 & -1 & 0 & 0 & 0 & 0 & 0 & 0 & 0 & \dots \\ 1 & 0 & 0 & 0 & 0 & 0 & 0 & 0 & 0 & \dots \\ 0 & 0 & 0 & -1 & 0 & 0 & 0 & 0 & 0 & \dots \\ 0 & 0 & 1 & 0 & 0 & 0 & 0 & 0 & 0 & \dots \\ 0 & 0 & 0 & 0 & 0 & 0 & 0 & 0 & 0 & \dots \\ 0 & 0 & 0 & 0 & 0 & 0 & -1 & 0 & 0 & \dots \\ 0 & 0 & 0 & 0 & 0 & 1 & 0 & 0 & 0 & \dots \\ 0 & 0 & 0 & 0 & 0 & 0 & 0 & 0 & -2 & \dots \\ 0 & 0 & 0 & 0 & 0 & 0 & 0 & 2 & 0 & \dots \\ \vdots & \vdots & \vdots & \vdots & \vdots & \vdots & \vdots & \vdots & \vdots & \ddots \end{pmatrix}. \quad (52)$$

In addition to the rotational symmetry, the pilot wave model with a central force is also equivariant under the reflection  $y \rightarrow -y$ , or equivalently  $\theta \rightarrow -\theta$ . The action of this transformation on the state space coordinates is represented by the diagonal matrix

$$\sigma = \text{diag}[1, -1, 1, -1, 1, 1, -1, 1, -1, \dots], \quad (53)$$

and the finite-time flow mapping implied by the time-evolution under (44–47) satisfies

$$f^\tau(\sigma a) = \sigma f^\tau(a). \quad (54)$$

The model parameters (48) are determined by the experimental conditions as explained by Oza *et al.*<sup>12</sup> and Perard *et al.*<sup>10</sup>. In the following numerical work, we are going to adopt the numbers reported by Tambasco *et al.*<sup>13</sup> and set  $m = 0.25 \times 10^{-6} \text{ kg}$ ,  $f = 80 \text{ Hz}$ ,  $D = 2.0 \times 10^{-6} \text{ kg/s}$ ,  $A = 3.5 \times 10^{-6} \text{ m}$ , and  $k = 3.2 \times 10^{-6} \text{ N/m}$ . These choices yield the nondimensional system parameters

$$\eta = 0.2, \quad \chi = 0.008, \quad \mu = 0.0375482401231. \quad (55)$$

In the next section, we are going to explore the bifurcations of this model and the onset of chaos numerically for  $Me \in [10, 19]$ . We observed for this parameter range that a truncation of the Fourier-Bessel expansion (30) at  $N = 25$  ensures at least 8 order of magnitude drop in the mode amplitudes  $\|C_n + S_n\|$ , hence the numerical results that we are going to report adopts this resolution. Note that the resulting state space representation is 55-dimensional. In the numerical results to follow, we simulate this 55-dimensional ODE system (44–47) using `odeint` function of `scipy.integrate` module<sup>32</sup> of Python programming language. Note that `odeint` adapts the time-steps in order to keep estimated numerical integration errors below  $10^{-8}$ . In the results of the following sections, the trajectories are sampled with a time-step  $\delta\tau = 0.01$ . For simulations in the symmetry-reduced state space, we integrate (19), which we obtain explicitly by projecting (44–47).

### III.1. Local bifurcations and the onset of chaos

As we shall now demonstrate, the explicit ODE form of the dynamical equations (44–47) along with the symmetry reduced dynamics (20–21) allow us to use standard numerical analysis methods for a bifurcation study of the pilot-wave system. In this section and the rest of the paper, we are going to use the following naming convention for the solutions we describe. Initial capital letters will refer to the type

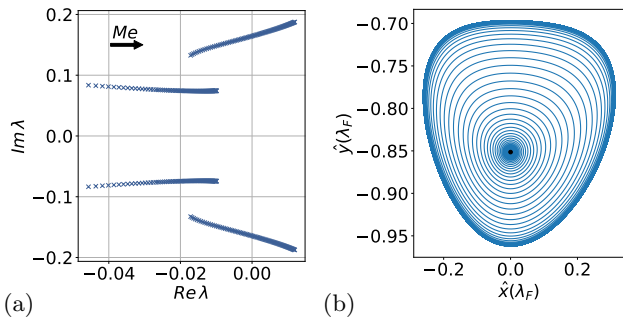


FIG. 3. Destabilization of the circular trajectory with increasing  $Me \in [10, 19]$ . (a) Real and imaginary parts of the leading two pairs of complex conjugate stability eigenvalues of the circular trajectory. Direction of the increasing memory is indicated by the annotated arrow. (b) An orbit with the initial condition (56) at  $Me = 15$  illustrating the connection of the unstable manifold of REQ0c (marked black) to RPO1o.

of the solution: EQ: equilibrium, REQ: relative equilibrium, PO: periodic orbit, RPO: relative periodic orbit, C: chaotic. The following integer (except for chaotic solutions) will refer to the number of times the solution intersects the Poincaré section (60), which we are going to define and use for our illustrations later. The following lowercase letter will refer to the shape of the solution on the  $(x, y)$ -plane: c: circle, o: oval, l: lemniscate, t: trefoil. The solutions that are not reflection-symmetric will appear in pairs of positive and negative average angular momenta. We will refer to the ones with negative average angular momentum with an additional  $\sigma$  in front. For example, the circular solution is a relative equilibrium that does not intersect the Poincaré section (60); thus, the circular solution with positive angular momentum will be REQ0c and its reflection copy with negative angular momentum will be  $\sigma$ REQ0c. When needed, additional letters will be used to further specify the solutions and these will be explained in place. For reference, table I shows a summary of invariant solutions in the numerical bifurcation study to follow. In table I and the rest of the trajectory plots of this paper, the lengths are scaled by  $2\pi$  so that one unit of distance is equal to one Faraday wavelength.

### III.1.1. Bifurcations from the circular solution

As shown by Labousse *et al.*<sup>27</sup> and Tambasco *et al.*<sup>13</sup>, when  $Me = 10$ , the dynamical system described by (44–47) has a stable circular orbit with radius  $r \approx 0.8\lambda_F$ , which we have visualized in figure 1. This solution is a relative equilibrium (7), which we are going to refer to as REQ0c. REQ0c intersects the slice hyperplane (15) at a single point  $\hat{a}_{\text{REQ0c}}$  corresponding to the snapshot on figure 1(a). This solution satisfies the equilibrium condition (22) in the symmetry-reduced state space. Starting from the stable  $\hat{a}_{\text{REQ0c}}$  at  $Me = 10.0$ , we increased the  $Me$  in steps of 0.1, find the root of (22) numerically using `fsolve` function from `scipy.optimize`<sup>32</sup> and compute the spectrum of (24) at this point for each  $Me$  value. In these computations, we discarded the 4<sup>th</sup> column of  $\hat{v}(\hat{a})$ , which corresponds to the  $\hat{v}_y$  direction that is identically set to 0 in the slice. Similarly, when computing the eigenvalues of (24) we discard the 4<sup>th</sup> column and row.

The leading (with the largest  $\text{Re } \lambda$ ) two pairs of linear stability eigenvalues of the circular trajectory computed this way are plotted in figure 3(a). As shown, the leading pair of complex conjugate eigenvalues  $\lambda_{1,2}$  cross the imaginary axis upon increasing  $Me$ . This corresponds to the interval  $Me \in (13.7, 13.8)$  and at  $Me = 13.8$ , the circular trajectory is unstable. For verification, we translated this  $Me$  value to the to the forcing acceleration  $\gamma$  which is related to  $Me$  by  $Me T_F = T_d / (1 - \gamma / \gamma_F)$ , where  $T_d$  is the decay time of waves in the absence of forcing and  $\gamma_F$  is the Faraday instability threshold. With  $T_F = 2/f = 0.025s$  and  $T_d \approx 0.0182^{27}$ ,  $Me = 13.8$  corresponds to  $\gamma / \gamma_F \approx 0.9472$ . This value is in agreement with Tambasco *et al.*<sup>13</sup> who reported the destabilization of the circular orbit at  $\gamma / \gamma_F = 0.948$ .

The destabilization of the circular orbit as  $Me$  is increased corresponds to a supercritical Hopf bifurcation as we confirm by the appearance of a relative periodic orbit in its vicinity. This is illustrated in figure 3(b), where we show an orbit at  $Me = 15$  starting approximately on the unstable manifold of REQ0c with the initial condition

$$\hat{a}(0) = \hat{a}_{\text{REQ0c}} + 10^{-4} \text{Re } \hat{e}_1. \quad (56)$$

In order to find this relative periodic orbit to the numerical precision, we implemented Newton’s method (Appendix A) for periodic orbits to find the roots of (25). Once again, discarding the 4<sup>th</sup> element of the equation, which is set to 0 by the symmetry reduction. We visualized the relative periodic orbit’s trajectory on  $(x, y)$  plane along with the corresponding wave field at  $Me = 15$  as three snapshots in figure 4. Perard *et al.*<sup>10</sup> referred to the orbits with similar trajectories as “ovals”, which we will also adopt for the family of solutions to follow. At  $Me = 15$ , RPO1o is stable and its period is  $T_{\text{RPO1o}} \approx 40.04$ , thus, snapshots in figure 4(a) and (c) are approximately one period apart. Notice that the wave fields in figure 4 (a) and (c) are almost the same up to a rotation of the coordinates.

As we did with the circular solution, we varied  $Me \in [14, 19]$  with steps of 0.1 and numerically solved (25) using Newton’s method and obtained the Floquet multipliers of RPO1o by computing the eigenvalues of (26) at each step. We plotted the leading (with largest  $|\Lambda_i|$ ) three Floquet multipliers of RPO1o for  $Me \in [14, 19]$  on figure 5(a). For each  $Me$  value, there is a marginal Floquet multiplier with  $\Lambda = 1$  corresponding to the perturbations along the periodic orbit, as expected. Leading non-marginal pair of complex conjugate Floquet multipliers cross the unit circle at  $Me \in (16.8, 16.9)$  (annotated in figure 5(a)) and after this point, RPO1o is unstable.

In order to study the dynamics on the  $(\text{Re } V_1, \text{Im } V_1)$ -plane in the vicinity of  $\hat{a}_{\text{RPO1o}}$  after it becomes unstable, we define a Poincaré section as the half-hyperplane

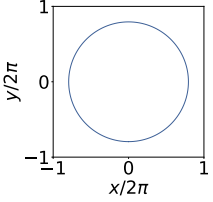
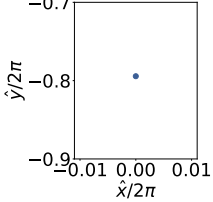
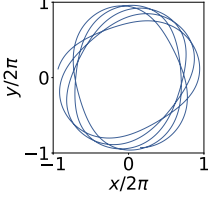
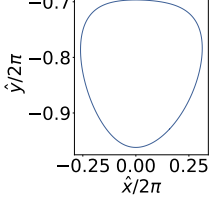
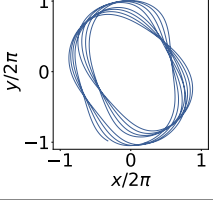
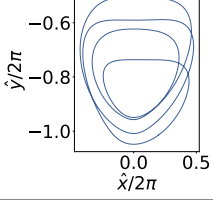
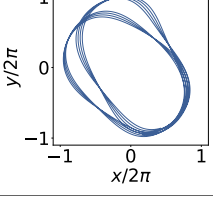
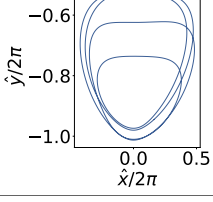
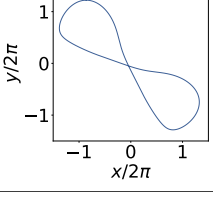
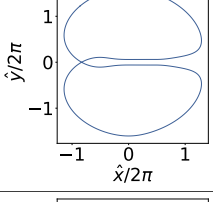
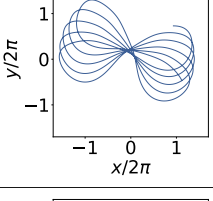
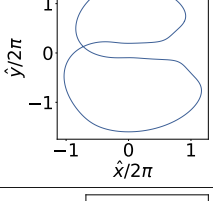
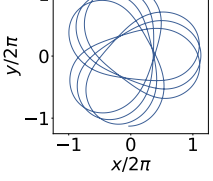
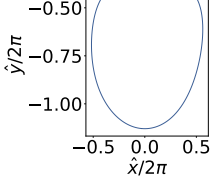
$$\langle \hat{a}_{\mathcal{P}} - \hat{a}_{\text{RPO1o}}, \hat{v}(\hat{a}_{\text{RPO1o}}) \rangle = 0, \quad \langle \hat{v}(\hat{a}_{\mathcal{P}}), \hat{v}(\hat{a}_{\text{RPO1o}}) \rangle > 0, \quad (57)$$

where  $\hat{a}_{\text{RPO1o}}$  is an arbitrary point on RPO1o and  $\hat{a}_{\mathcal{P}}$  denotes the state space points on the Poincaré section. We started a simulation with the initial condition

$$\hat{a}(0) = \hat{a}_{\text{RPO1o}} + 10^{-4} \text{Re } V_1 \quad (58)$$

and tracked its intersections with the Poincaré section (57). In order to visualize the dynamics on this Poincaré section, we projected it onto the orthonormal bases  $(\hat{\xi}_1, \hat{\xi}_2)$  that span the  $(\text{Re } V_1, \text{Im } V_1)$ -plane in figure 5(b) at  $Me = 17$ . As suggested by the appearance of an invariant 2-torus in the vicinity

TABLE I. Summary of invariant pilot-wave solutions that are studied in this paper. Each solution has a reflection-copy with the exception of PO2l, which itself is symmetric under the reflection (53). The last column shows the  $Me$  value at which the trajectories are plotted.

Name	Type	Shape	Trajectory	Reduced trajectory	at $Me$
REQ0c	Relative equilibrium	Circle			10.0
RPO1o	Relative periodic orbit	Oval			15.0
RPO4os	Relative periodic orbit	Oval			18.0
RPO4ou	Relative periodic orbit	Oval			18.0
PO2l	Periodic orbit	Lemniscate			14.0
RPO2l	Relative periodic orbit	Lemniscate			16.0
RPO1t	Relative periodic orbit	Trefoil			14.0



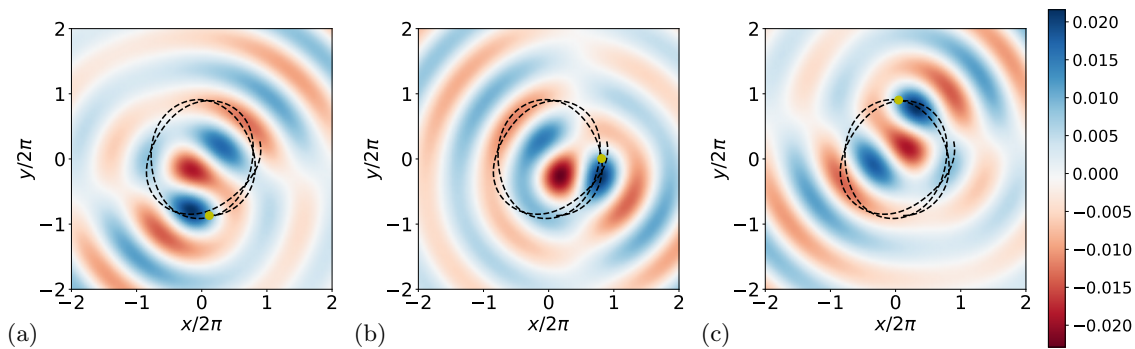


FIG. 4. Three snapshots of a simulated trajectory of RPO1o where the trace of the droplet for five periods is drawn as a dashed curve and its instantaneous position at the respective snapshot is indicated with a yellow dot in each figure. The magnitude of the wave field color coded in each snapshot. (a)  $\tau = 0$ , (b)  $\tau = 20$ , (c)  $\tau = 40$ .

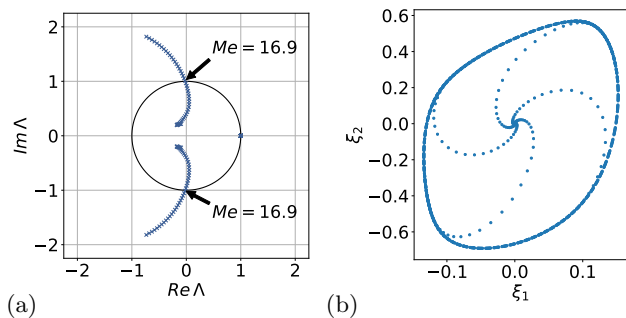


FIG. 5. Destabilization of the RPO1o with increasing  $Me \in [14, 19]$ . (a) Real and imaginary parts of the leading three Floquet multipliers of RPO1o.  $Me = 16.9$  at which the leading complex conjugate Floquet multipliers cross the unit circle is annotated. (b) An orbit with the initial condition (58) at  $Me = 17$  illustrating the connection of RPO1o's unstable manifold to the surrounding 2-torus as a projection from the Poincaré section (57).

of RPO1o, its leading complex conjugate Floquet multipliers' crossing of the unit circle corresponds to a supercritical Neimark-Sacker bifurcation<sup>33</sup>.

The invariant 2-torus surrounding RPO1o disappears at  $Me \in (17.1, 17.2)$  and leaves its place to a stable and unstable pair of period-4 (on the Poincaré section) orbits. In order to elucidate this process, we analyzed the system before ( $Me = 17.1$ ) and after ( $Me = 17.2$ ) the bifurcation. At  $Me = 17.1$ , we parameterized the invariant torus surrounding RPO1o with  $\theta_{\mathcal{P}} \in [0, 2\pi)$  and generated a return map  $\theta_{\mathcal{P}}[n+1] = f_{\mathcal{P}}(\theta_{\mathcal{P}}[n])$  as shown in figure 6(a). Upon our investigation of the fourth iterate of this map, we have found that at 4 locations it comes close to being tangent to the identity map as plotted in figure 6(b). This is a typical situation as the system proceeds towards a saddle-node bifurcation that would give rise to a stable-unstable pair of period-4 orbits. In order to elucidate the dynamics after this bifurcation, we approximated RPO1o's unstable manifold by forward integrating the initial conditions

$$\hat{a}(\delta, \phi) = \hat{a}_{\text{RPO1o}} + \epsilon \Lambda_1^\delta (\text{Re } V_1 \cos \phi + \text{Im } V_1 \sin \phi), \quad (59)$$

where we used 4-equidistant values for  $\delta \in [0, 1)$ , 36-equidistant values for  $\phi \in [0, 2\pi)$  and set  $\epsilon = 10^{-4}$ . Time-

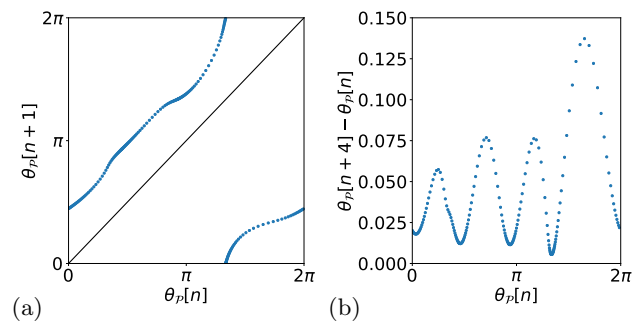


FIG. 6. (a) Poincaré return map of the dynamics on the 2-torus surrounding RPO1o at  $Me = 17.1$ . (b) Intersection of the 4-th iterate of the return map in (a) and the identity map, illustrating the map's progress towards a period-4 resonance.

forward dynamics of the initial conditions (59) approximately cover the linearized unstable manifold of RPO1o, thus we expect their further evolution to take the shape of the nonlinear unstable manifold<sup>16</sup>. We visualized these orbits at their intersections with the Poincaré section (57) as projections onto  $(\text{Re } V_1, \text{Im } V_1)$ -plane on figure 7. We found that all of these trajectories converged to a new stable periodic orbit (marked magenta on figure 7) that intersects the Poincaré section 4 times. We will refer to this orbit as RPO4os with the additional “s” signifying that this solution appears as the stable one of a saddle-node pair. We have also observed that this manifold was separated in two parts at 4 different locations, where nearby trajectories went in opposite directions when they arrived at the edge of the manifold as illustrated by red and black orbits on figure 7. By utilizing a Newton search, we confirmed that these separation points corresponded to an unstable period-4 orbit RPO4ou (“u” standing for “unstable”), which we marked yellow on figure 7. These observations together confirm that a saddle-node bifurcation on the invariant torus surrounding RPO1o took place at  $Me \in (17.1, 17.2)$ .

We then continued both RPO4ou and RPO4os up to  $Me = 19.0$ . For this computation, we needed to implement pseudoarclength continuation<sup>34</sup> since RPO4ou underwent several fold bifurcations and became more and more unstable. RPO4os, on the other hand, underwent a period doubling bifurcation at  $Me \in (17.8, 17.9)$ , marking the beginning of the

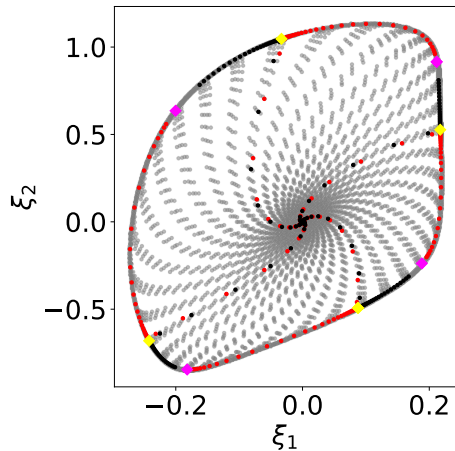


FIG. 7. The unstable manifold of RPO1o (at the center) at  $Me = 17.2$  visualized as the intersections (gray dots) of the time-forward dynamics of initial conditions (59) with the Poincaré section (57). Stable (RPO4os) and unstable (RPO4ou) pair of period-4 orbits are marked respectively with magenta and yellow diamonds. Two orbits that lie on different sides of RPO4ou’s stable manifold and then follow its unstable manifold in opposite directions marked red and black.

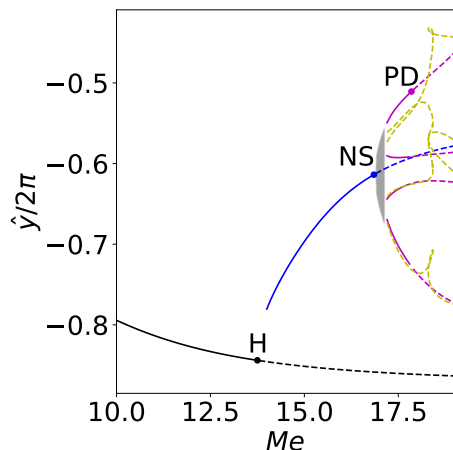


FIG. 8. Diagram summarizing bifurcations starting from the circular solution, where stable solutions are drawn as solid curves and unstable ones are dashed. Approximate bifurcation points are annotated with letters indicating the type of bifurcation; H: Hopf, NS: Neimark-Sacker, PD: Period doubling. Different colors correspond to different solutions; black: REQ0c, blue: RPO1o, gray(transparent): invariant torus, magenta: RPO4os, yellow: RPO4ou.

cascade which leads to chaos.

Until the period doubling point, the bifurcation sequence we described here qualitatively<sup>2</sup> agrees with the observations

of Tambasco *et al.*<sup>13</sup>, who studied the same system with a different numerical method. Notably, they also observed that the relative two-torus is replaced by a period-4 relative periodic orbit, which they refer to as “a frequency-locked wobbling orbit”. Upon further increase of  $Me$ , Tambasco *et al.*<sup>13</sup> observes a new incommensurate frequency in the Fourier spectrum of the wobbling orbit, which does not agree with the period doubling bifurcation we find here. Consequently Tambasco *et al.*’s description of transition to chaos disagrees with ours, which we will present in section III.2. In section IV, we discuss the differences between two transition scenarios in more detail.

We summarized the bifurcations that we analyzed up to this point in figure 8. The vertical axis of figure 8 shows the  $\hat{y}$  coordinate of  $\hat{a}_{REQ0c}$  and for the rest of the solutions, the  $\hat{y}$  coordinate of their intersections with the Poincaré section defined as the half-hyperplane

$$\langle \hat{a}_{\mathcal{P}_y} - \hat{t}_{\mathcal{P}_y}, \hat{n}_{\mathcal{P}_y} \rangle = 0, \quad \langle \hat{v}(\hat{a}_{\mathcal{P}_y}), \hat{n}_{\mathcal{P}_y} \rangle > 0 \quad (60)$$

where  $\hat{t}_{\mathcal{P}_y} = (0, 1, 0, \dots)$  and  $\hat{n}_{\mathcal{P}_y} = (1, 0, 0, \dots)$ . The Poincaré section (60) is equivalent to marking the reduced state space trajectories’ intersections with the  $\hat{y}$ -axis in  $+\hat{x}$  direction.

At the period doubling bifurcation of RPO4os, annotated with PD in figure 8, a period-8 cycle appears in its vicinity, which itself undergoes another period doubling upon further increase in  $Me$ . We postpone the analysis of the chaotic attractor, which forms following this cascade of period doublings to section III.2, and turn our focus to another set of solutions that coexist with the ones we presented so far.

### III.1.2. The lemniscate solution and the symmetry breaking

In the previous section, we followed primary and subsequent bifurcations from the counterclockwise rotating circular solution. All the solutions we presented so far had positive angular momentum  $L = xv_y - yv_x > 0$  at all times. Since the system is equivariant under the reflection symmetry (53), all of these solutions have reflection-symmetric counterparts with  $L < 0$ . A different type of stable periodic solution, which we will refer to as PO2l coexist in the state space at  $Me = 14.0$ . This solution can be found by initiating a simulation with a random initial condition at  $Me = 14.0$ : We observed at this regime that an initial condition  $a(0)$  that is populated by standard normally distributed numbers eventually lands on PO2l, or RPO4 (or its reflection copy  $\sigma$ RPO4). Both of these orbits are stable at  $Me = 14.0$ .

We visualized three snapshots from one full period of PO2l in figure 9. Perrard *et al.*<sup>10</sup> called similar solutions “lemniscates”, referring to their figure-8 shape. From figure 9, it can be seen that the droplet’s angular momentum is reversed as it traverses through one full period. In fact, the angular momentum along PO2l is exactly zero as the second half of the orbit is the reflection symmetry of the first half. Similar solutions of the Kuramoto-Sivashinsky system are sometimes

<sup>2</sup> The exact bifurcation points are slightly different, which could

be due to differences in the numerical methods.

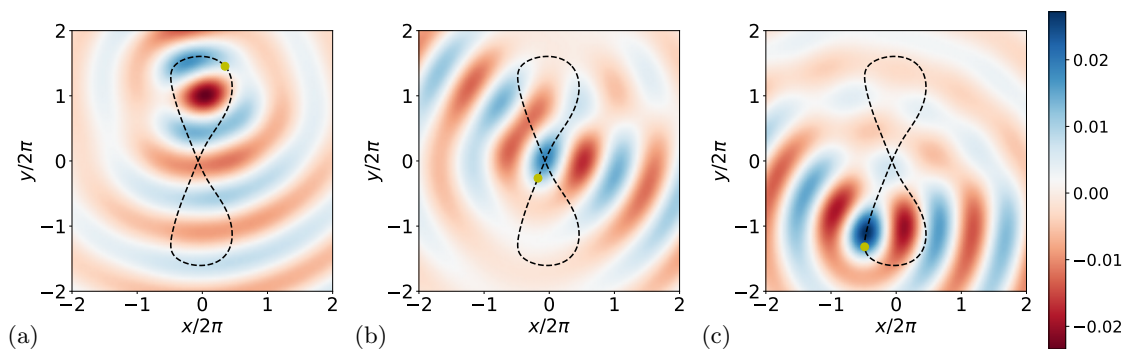


FIG. 9. Three snapshots of a simulated trajectory of PO2l at  $Me = 14.0$ . The trace of the droplet for one period is drawn as a dashed curve and its instantaneous position at the respective snapshot is indicated with a yellow dot in each figure. The magnitude of the wave field color coded in each snapshot (a)  $\tau = 0$ , (b)  $\tau = 25$ , (c)  $\tau = 50$ .

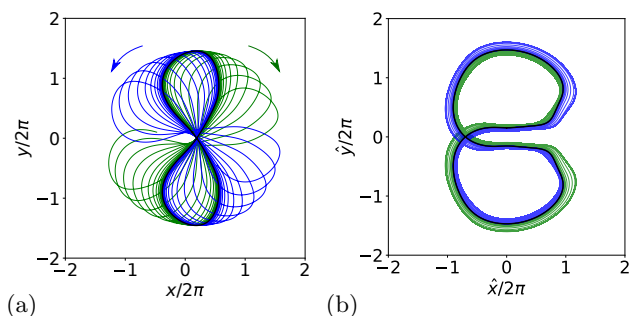


FIG. 10. PO2l (black) at  $Me = 16.0$  and symmetry-broken dynamics on its unstable manifold illustrated as the trajectories of perturbations to PO2l in  $\pm V_1$  (green/blue) directions; (a) in full state space, (b) after continuous symmetry reduction. Azimuthal drift directions of blue and green orbits are indicated with arrows in (a).

referred to as “pre-periodic”<sup>15,16</sup> since they can be treated as relative periodic orbits satisfying

$$a_{PO} = \sigma f^{T_{PO}/2}(a_{PO}). \quad (61)$$

In other words, after half period  $T_{PO}/2$ , the periodic orbit comes to the reflection of its initial position. Such solutions generically do not undergo period doubling bifurcations<sup>35</sup> and when the Jacobian of (61) has a negative real eigenvalue outside the unit circle, this corresponds to the symmetry-breaking.

A symmetry-breaking bifurcation of PO2l takes place at  $Me \in (15.6, 15.7)$  and there appears drifting lemniscate solutions in its vicinity. We visualized these dynamics in figure 10 by showing the trajectories of small perturbations  $\pm 10^{-2}V_1$  to PO2l, where  $V_1$  is the leading (unstable) Floquet vector. Figure 10 (a) shows the symmetry-broken dynamics in full state space along with the unstable PO2l. In figure 10 (b), when the symmetry is reduced, it becomes apparent that two new relative periodic orbits appear in PO2l’s vicinity. We are going to refer to these drifting lemniscates as RPO2l and  $\sigma$ RPO2l.

At  $Me \in (16.5, 16.6)$ , RPO2l undergoes a period doubling bifurcation, which leads to a cascade and a chaotic attractor formation. Before examining these dynamics in section III.2,

we must present another type of solution, which coexist with the ones we studied so far.

### III.1.3. The trefoil

In the previous section, we have stated that at  $Me = 14.0$ , the pilot-wave system has two stable solutions, RPO1o and PO2l, and a random initial condition eventually lands on one or the other. A natural question to ask at this stage is the following. What separates the basins of attraction of these two solutions? Experience from previous studies<sup>36–38</sup> of low dimensional systems suggests that such disconnected regions might be separated by the stable manifold of another invariant solution. One of the most prominent examples of this kind of state space structure is manifested in the subcritical transition to turbulence in shear flows, where laminar and turbulent flows are coexisting attractors. In numerical simulations of channel flow, Itano and Toh<sup>39</sup> were first to find a traveling wave solution (a relative equilibrium) by a shooting method which bisects between trajectories whose energy fluctuations eventually reach turbulent levels and those that vanishes. This suggested that the turbulent and laminar regions of the state space were separated by the stable manifold of this solution. Following numerical studies<sup>40–46</sup> of shear flows found similar solutions<sup>3</sup> with shooting methods akin to the one used by Itano and Toh<sup>39</sup>. Such separating solutions in subcritical transition literature are now generally referred to as “edge states”, following the terminology introduced by Schneider *et al.*<sup>41</sup> and the bisection methods for locating them is usually called “edge tracking”. We are going to adopt this terminology in what follows.

In order to investigate the edge between the initial conditions that eventually land on RPO1o and those that go to PO2l, we formulated the following edge tracking method. For tracking the laminar-turbulent boundary in shear flows, the kinetic energy of turbulent fluctuations is usually used as a proxy to determine whether the solution eventually becomes turbulent. In our case, we found the time-averaged angular

<sup>3</sup> The exact type of the invariant solution depends on the system under study and the parameters.

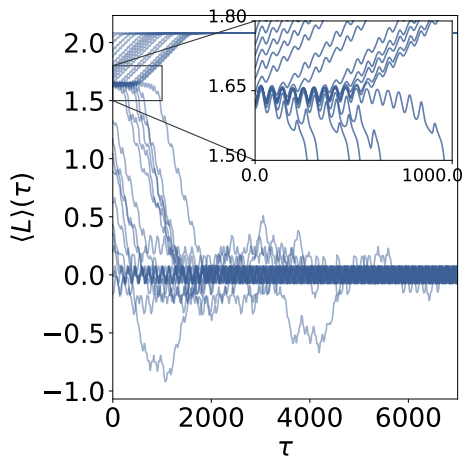


FIG. 11. Time-series of the window-averaged angular momentum of bisection trajectories. Inset: Zoom-in showing nearly-periodic temporal dynamics.

momentum of the final state to be an appropriate quantity and formulated the edge tracking algorithm in appendix B.

Let  $\hat{a}_{\text{RPO1o}}$  and  $\hat{a}_{\text{RPO1o}}$  be random points on RPO1o and PO2l. In order to search for the basin boundary between PO2l and RPO1o, we run edge tracking algorithm (appendix B) with  $\epsilon = 10^{-9}$ ,  $\tau_f = 10000$ ,  $\tau_w = 1000$ ,  $L_{th,1} = 1.8$ ,  $L_{th,2} = 0.1$ . We plotted the time-series of the window-averaged angular momentum in figure 11. As expected, the average angular momentum eventually settles around  $\langle L \rangle \approx 0$  (PO2l) or  $\langle L \rangle \approx 2.1$  (RPO1o). Notice, however, that before landing on these final states, the average angular momentum of the bisection trajectories oscillates around  $\langle L \rangle \approx 1.65$ . We observed approximately periodic symmetry-reduced dynamics in these episodes; and upon a Newton search, found a new relative periodic orbit, which we will refer to as RPO1t.

In Figure 12, we visualize three snapshots from RPO1t’s trajectory simulated in the full state space. Experimentally observed solutions with similar shapes were named “trefoils” by Perrard *et al.*<sup>10</sup>. By numerical continuation, we confirmed that when  $Me \in [12.91, 19.0]$ , RPO1t has one positive Floquet multiplier outside the unit circle, which renders RPO1t’s stable manifold codimension-1. This is in agreement with our initial intuition since a codimension-1 manifold divides the state space into two distinct regions. Thus, we conclude that at  $Me = 14.0$ , the edge between the basins of attraction of RPO1o and PO2l is set by the stable manifold of the trefoil solution RPO1t.

RPO1t appears in a saddle-node bifurcation at  $Me \approx 12.91$  along with a stable branch, trajectory of which is also trefoil-shaped. We observed this stable solution for  $Me \in [12.91, 12.95]$ , however, our efforts in continuing this solution to higher  $Me$  have failed. Trefoil-shaped trajectories have been observed in both laboratory<sup>10</sup> and numerical<sup>28</sup> experiments, which could only be possible if the associated solution is stable. Our observation of the stable trefoil orbit following the saddle-node bifurcation provides one explanation for experimental findings by fine-tuning the system parameters and initial conditions. It is conceivable that other trefoil-shaped solutions might appear at saddle-node bifurcations at different parameter values.

### III.2. Chaotic attractors and their global bifurcations

In the previous sections, we showed that the droplet system has three different families of solutions: (1) the circular solution and the subsequent ovals, (2) the lemniscate solutions, and (3) the trefoil. We have already mentioned that two of these solutions, namely RPO4os and RPO2l, undergo period-doubling bifurcations. In this section, we are going to illustrate that both of these period-doublings yield chaotic dynamics, which subsequently merge and generate full complexity of the chaotic pilot-wave dynamics.

The first set of period doublings take place in the neighborhoods of RPO2l and its reflection symmetry  $\sigma$ RPO2l. In order to illustrate these bifurcations, we generated the orbit diagram in figure 13, where we plotted the  $\hat{y}$  coordinate of the very long trajectories’ intersections with the Poincaré section (60). Starting at  $Me = 16.0$  with initial conditions on RPO2l and  $\sigma$ RPO2l, we increased  $Me$  in steps of 0.001, used the final state of the previous step as the initial condition of the next step, and generated a long data set. Figure 13 shows the intersections of these trajectories with the Poincaré section (60) after initial transients are discarded. Green markers correspond to orbits that started from RPO2l and the blue ones correspond to the ones that started from  $\sigma$ RPO2l. Additionally, the symmetric lemniscate PO2l is shown as black dashed lines, and the trefoil solutions RPO1t and  $\sigma$ RPO1t are drawn as yellow dashed lines.

The first period doubling of RPO2l and  $\sigma$ RPO2l takes place at  $Me \approx 16.437$ . This bifurcation is followed by a cascade of period doublings, which yields chaotic sets C1 and  $\sigma$ C1 in the vicinity of RPO2l and  $\sigma$ RPO2l, respectively. As illustrated in figure 10, these two reflection-related regions are separated by PO2l (drawn dashed black in figure 13) and we observed that the two chaotic regions merge at  $Me \approx 16.580$ , as they cross the border set by PO2l. At this point, the chaotic attractors, which are symmetry-copies of one another merge through a symmetry-increasing bifurcation<sup>47</sup> and result in a reflection-symmetric attractor  $C1 = \sigma C1$ .

Upon further increase of  $Me$ , we observed that when  $Me > 16.616$ , the long trajectories eventually leave this chaotic neighborhood and settle on RPO1o or  $\sigma$ RPO1o, which are stable until  $Me \approx 16.9$ , see figure 5. This suggests that the chaotic attractor crosses the stable manifold of RPO1t, which sets the boundary between the neighborhoods of RPO2l and RPO1o. At the first glance, approach of the chaotic attractor towards RPO1t is not obvious, however, when we zoomed into the parameter region  $Me \in [16.6, 16.616]$  (the inset of figure 13), we observed that the chaotic dynamics came close to RPO1t. These visits are rather rare: We observed only a few instances in more than 3500 intersections with the Poincaré section (60) at  $Me = 16.616$ . The sudden transition from a chaotic attractor to a chaotic transient is called a “boundary crisis”<sup>36,38</sup>. It is not clear from our data whether or not the expansion of the attractor towards RPO1t is continuous. Nevertheless, we believe that around  $Me \in (16.616, 16.617)$ , a boundary crisis causes the destruction of this chaotic attractor. For further evidence, we carried out a bisection search similar to that of figure 11 at  $Me = 16.6$  and found, once again, that RPO1t to be the edge state in between the neighborhoods of RPO2l and RPO1o.

In section III.1.1, we have shown that upon the increase of  $Me$ , RPO1o first undergoes a Neimark-Sacker bifurcation and as we further increased the  $Me$ , the invariant torus in the

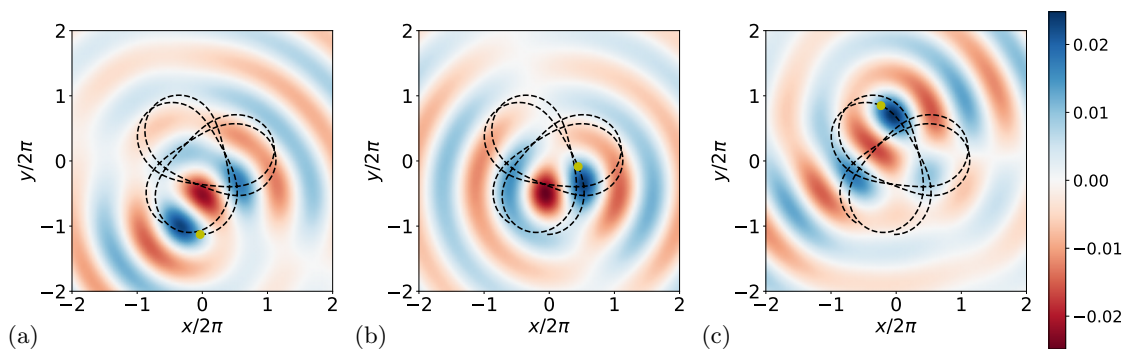


FIG. 12. Three snapshots of a simulated trajectory of RPO1t at  $Me = 14.0$ . The trace of the droplet for six periods is drawn as a dashed curve and its positions at the instance of snapshots are indicated with a yellow dot at each figure. The magnitude of the wave field at the instance of snapshot is color coded. (a)  $\tau = 0$ , (b)  $\tau = 20$ , (c)  $\tau = 40$ .

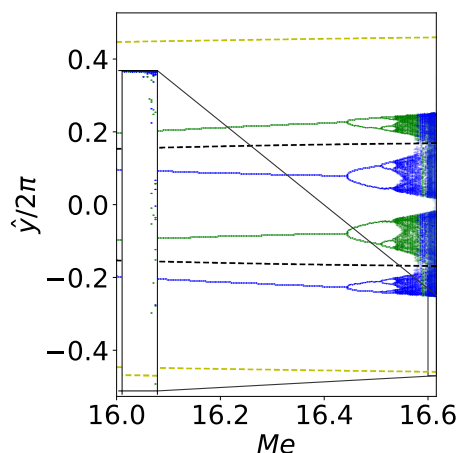


FIG. 13. Orbit diagram illustrating the period doubling cascade to chaos in the neighborhoods of RPO2l (green) and  $\sigma$ RPO2l (blue). The symmetric-lemniscate PO2l and the trefoil solutions RPO1t and  $\sigma$ RPO1t are shown as black and yellow dashed-lines. Inset: zoom-in to the lower-right corner to illustrate the rare visits of chaotic dynamics to the neighborhood of RPO1t.

neighborhood of RPO1o is replaced the stable and unstable manifolds of a pair of period-4 orbits RPO4os and RPO4ou. We ended section III.1.1 by mentioning that RPO4os, which is initially stable, undergoes a period doubling bifurcation at  $Me \in (17.8, 17.9)$ . We illustrated the following cascade of period-doublings and the emergence of chaotic dynamics on the orbit diagrams of figure 14

Similar to figure 13, we produced figure 14 by recording the intersections of long trajectories with the Poincaré section (60) after discarding the initial transients for  $Me \in [17.8, 19.0]$ . At  $Me = 17.8$ , we started with an initial condition on RPO4os and for the following simulations, we used the final point of the last step as the initial condition. Figure 14 illustrates the results of these simulations, where we show the  $\hat{y}$  values where trajectories intersect (60) at different  $Me$ . For clarity, we did not show the bifurcations of  $\sigma$ RPO4os on figure 14, but one should keep in mind that the same cascade also takes place in the vicinity of  $\sigma$ RPO4os.

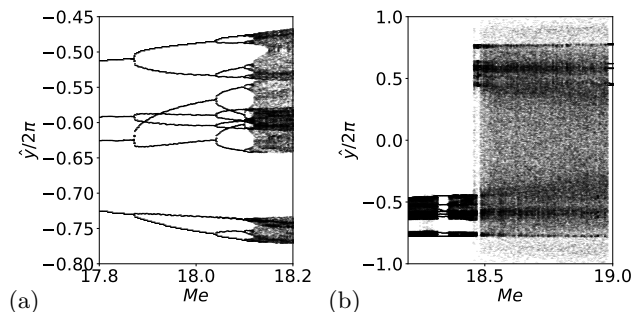


FIG. 14. Orbit diagrams visualizing (a) the period doubling cascade to chaos starting from RPO4os, (b) the symmetry-increasing bifurcation at  $Me \approx 18.455$  leading to sudden expansion of the chaotic attractor.

Three consecutive period doublings are visible in figure 14(a) and more can be found by zooming into smaller parameter regions. This result shows that the transition to chaos in this system follows a typical period-doubling route as opposed to Ruelle-Takens-Newhouse scenario<sup>48</sup>, which was previously suggested by Tambasco *et al.*<sup>13</sup>. We are going to refer to the resulting chaotic attractors as Co and  $\sigma$ Co.

As visualized in figure 14(b), dynamics of Co for  $Me > 18.2$  is chaotic with intermittent periodic windows, which is typical for attractors that follow a period doubling cascades<sup>49</sup>. Notice the sudden expansion of the chaotic attractor at  $Me \approx 18.455$ . This is another symmetry-increasing bifurcation where Co connects to its reflection symmetry  $\sigma$ Co yielding the final chaotic attractor of the pilot-wave system. As we shall now illustrate, this global bifurcation is indeed the result of the merging of Co and  $\sigma$ Co with Cl.

As we explained earlier, at  $Me \approx 16.617$ , Cl becomes unstable by merging with RPO1t. After this boundary crisis, Cl includes RPO1t and becomes the chaotic edge state between the attractors RPO1o and  $\sigma$ RPO1o. Cl carries this role up until  $Me \approx 18.455$ , when the distinct attractors are chaotic. We illustrated this in figure 15 at  $Me = 16.8$  and  $Me = 18.45$  where the red trajectories were obtained by edge tracking (appendix B) between solutions with positive and negative angular momenta. In both cases, red trajectories in figure 15 are chaotic transients that would fall onto one of the attractors if integrated long enough. Figure 15 (b) illustrates

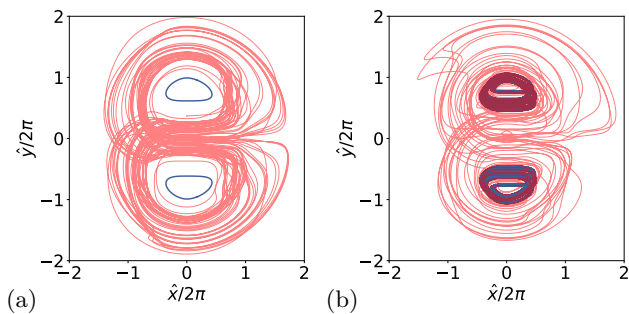


FIG. 15. (a) Chaotic edge state Cl (red) separating RPO1o (blue,  $\hat{y} < 0$ ) and  $\sigma$ RPO1o (blue,  $\hat{y} > 0$ ) at  $Me = 16.8$ . (b) Chaotic edge state Cl (red) separating Co (blue,  $\hat{y} < 0$ ) and  $\sigma$ Co (blue,  $\hat{y} > 0$ ) at  $Me = 18.45$ .

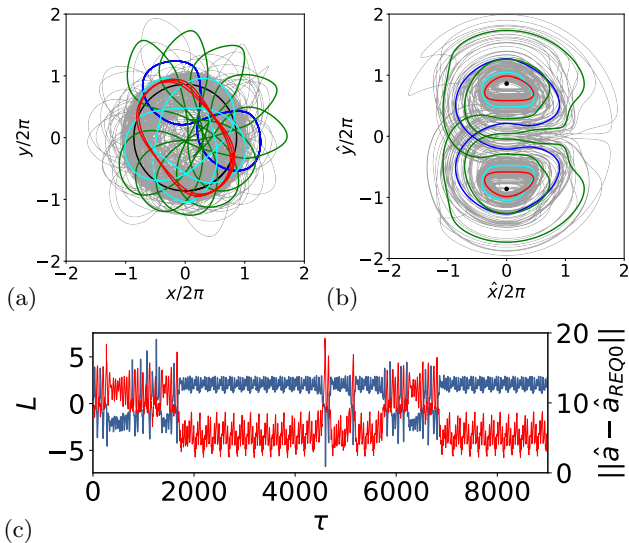


FIG. 16. Projections of the circular solution REQ0c (black), the (relative) periodic orbits RPO1o (red, oval), RPO1t (cyan, trefoil), PO2l (blue, lemniscate), RPO2l (green, lemniscate), and a long chaotic trajectory (gray) (a) in full state space onto the  $(x, y)$ -plane, (b) in the symmetry-reduced state space onto the  $(\hat{x}, \hat{y})$ -plane. 5-repeats of each relative periodic orbit is shown in (a). In (b), reflection-copies of the relative periodic orbits are also plotted with the same color. (c) The chaotically moving droplet's angular momentum (blue) and its distance from REQ0c (red) as functions of time.

the state space picture just before the merging of two chaotic regions. At this point, blue and red regions are still dynamically disconnected and their apparent overlap is due to the lower-dimensional projection.

Finally, we are going to present the chaotic attractor following the symmetry-increasing global bifurcation at  $Me \approx 18.455$ . After this point, two chaotic regions Co and  $\sigma$ Co are connected through Cl and the trajectories intermittently switch between these neighborhoods. We illustrate this dynamics in figure 16 where we plotted a long chaotic trajectory along with REQ0c, RPO1o, RPO1t, PO2l, RPO2l in the full state space (figure 16 (a)) and in the symmetry-reduced state space (figure 16 (b)) at  $Me = 18.5$ .

The chaotic attractor in figure 16 (b), which is revealed after the symmetry-reduction, is qualitatively similar to the well-known Lorenz attractor<sup>50</sup>. Akin to the counterclockwise-rotating circular solution REQ0c and its reflection-symmetry  $\sigma$ REQ0c, the Lorenz system at standard parameter values has two non-trivial equilibria that are related by a rotation by  $\pi$  and the dynamics chaotically switches between their neighborhoods. In the droplet system, the switchings between the neighborhoods of the circular solutions correspond to the reversal of the droplet's angular momentum. We illustrated this in the time-series of figure 16(c), where we show the chaotically moving droplet's angular momentum and its distance from REQ0c as functions of time. Since REQ0c's angular momentum is positive (counterclockwise rotation), when the trajectory is close to it, the droplet's angular momentum is positive and vice versa. This, in fact, is also visible from the projection of figure 16(b). Since the symmetry reduction (9) sets  $\hat{v}_y = 0$  and  $\hat{v}_x > 0$ , the angular momentum in the symmetry-reduced state space is  $L = -\hat{y}\hat{v}_x$  and its sign is the opposite of  $\hat{y}$ 's. Hence, the  $\hat{y} = 0$  hyperplane separates solutions with positive angular momenta from those with negative angular momenta in the symmetry-reduced state space.

Besides the chaotic attractor, we also visualized the invariant solutions of the pilot-wave system in figure 16 (a,b). It is clear from figure 16(b) that the oval (RPO1o) and the trefoil (RPO1t) solutions' angular momenta do not change sign along one period whereas the angular momenta of the lemniscates reverse twice in one full period. The chaotic trajectories' angular momentum reversals correspond to the episodes during which they are shadowed by the lemniscates.

#### IV. CONCLUSION AND DISCUSSION

In this paper, we introduced a continuous symmetry-reduction method for hydrodynamic pilot-wave systems with rotational symmetry. In essence, our method is fixing the polar-angle in the velocity plane  $(v_x, v_y)$  (as opposed to  $(x, y)$ -plane) in order to obtain a transformation that is nonsingular for generic dynamics. We formulated this transformation in such a way that it can be used to simplify both experimental and numerical data by eliminating the symmetry degeneracy of the solutions. We then proceeded to reformulate this transformation in the framework of the method of slices. This formulation brought us a set of geometrical tools, which are useful mainly for theoretical and computational undertakings. In order to demonstrate the utility of the introduced symmetry-reduction technique, we applied it to the numerical study of Oza *et al.*'s<sup>12</sup> trajectory equation with central harmonic forcing. With the help of the symmetry-reduction, we analyzed the bifurcations and the subsequent chaotic dynamics in this system.

The main message we would like to deliver is that the continuous symmetry reduction substantially simplifies the pilot-wave dynamics by eliminating infinitely many copies of each generic solution. This is perhaps best illustrated in figure 16, where the symmetry-reduction reveals a relatively simple chaotic attractor with qualitatively different regions. Moreover, the symmetry reduction allowed us to numerically identify the unstable invariant solutions and their roles in organizing the state space of the system.

In the previous experimental<sup>10,11</sup> and numerical<sup>28</sup> studies of hydrodynamic pilot-wave systems with central harmonic

forcing, invariant solutions such as circles, ovals, lemniscates, and trefoils, were observed by tuning system parameters to the values at which these solutions were stable. These papers also demonstrated that the chaotic solutions transiently resembled the invariant solutions, hence they conjectured that in the chaotic regime, the dynamics can be decomposed into episodes approximated by different invariant solutions. Our results essentially confirm this conjecture: The chaotic pilot-wave dynamics is a union of two chaotic state space regions that are formed in the vicinity of the oval and lemniscate solutions and these solutions persist in the chaotic regime, albeit they are unstable. This observation can potentially be brought to a quantitative level: Long-term averages of the observables associated with a chaotic system can be predicted from its periodic orbits if the system and periodic orbits satisfy certain properties such as ergodicity and hyperbolicity. The collection of methods to carry out such computations is known as the periodic orbit theory<sup>24,51</sup> and our results suggest that such a calculation can be done in this context. Hence, the periodic orbit analysis of chaotic pilot-wave systems is one of our future research directions.

Symmetries of the radially-confined pilot-wave systems were recognized in previous literature at varying levels. For example, Perrard et al.<sup>10</sup> noted that the symmetries of the droplet trajectories were reflected in the Fourier-Bessel decomposition of the bath's surface height. Durey & Milewski<sup>52</sup> observed that the perfect lemniscate solution had 0 mean angular momentum due to its reflection symmetry. Durey & Milewski<sup>52</sup> also used successive maxima of radius as the averaging window in their data analysis. Similarly, Perrard et al.<sup>11</sup> used successive maxima of the radius in order to construct a return map. The choice of radius as a diagnostic variable is inherently symmetry-related since the radius is an invariant of rotation and reflection. The main difference of our work against the previous techniques is that we do not only use symmetry-invariant variables for extracting information but also express the dynamics in terms of them. Thus, our symmetry-reduced representation retains all dynamical information.

Transition to chaos in the model studied here were also examined by Tambasco *et al.*<sup>13</sup> who conjectured that the chaotic dynamics appear following a Ruelle-Takens-Newhouse transition scenario<sup>48</sup>. Their conjecture was based on the observation of a three-frequency orbit (fig. 6d of ref.<sup>13</sup>) prior to chaos. However, as noted by the authors themselves, two frequencies  $f_1$  and  $f_2$  that are visible in the spectrum of this orbit are in fact commensurate, i.e.  $f_1 = 4f_2$ . Thus, even if the third frequency is incommensurate with the first two, the associated symmetry-invariant dynamics takes place on a two-torus which does not meet the necessary criterion for a Ruelle-Takens-Newhouse transition scenario<sup>48</sup>. Here, we found that the transition from the stable period-4 orbit RPO4os to chaos is a result of a period-doubling cascade, through which a new commensurate frequency appears at each bifurcation. We would like to note that the numerical method<sup>53</sup> adopted in ref.<sup>13</sup> is very different from ours: They integrate the integro-differential trajectory equation (27) with (29) using an explicit fourth-order Adams-Bashfort method with a fixed time-step. We, on the other hand, simulate a truncated ODE representation. In order to check our results' robustness against truncation at this regime, we quadrupled number of Fourier-Bessel modes and confirmed that we still observe period-doubled orbits prior to the chaos.

While we focused on pilot-wave systems in this paper, our

symmetry-related methods can be extended to a larger class of systems in which a finite-size (or point-like) object interacts with a continuous environment. Similarly, it could be possible to generalize our method to three-dimensional space by introducing Euler angles for polar coordinate transformations.

In summary, we have shown that the continuous symmetry reduction drastically simplifies the data generated by a hydrodynamic pilot-wave system with chaotic dynamics. To this end, we formulated a symmetry-reduction method and applied it to the numerical simulations of a rotation-equivariant pilot-wave model with a central harmonic force. We identified local bifurcations, the onset of chaos, and the global attractor merging bifurcations in the system; as well as a qualitative description of its state space geometry.

## ACKNOWLEDGEMENT

We acknowledge stimulating discussions with Predrag Cvitanović and Matthieu Labousse. We are grateful to George Choueiri for his critical reading of an early version of this manuscript.

## Appendix A: Newton's method

Let  $(\hat{a}_{\text{RPO}}^{(i)}, T_{\text{RPO}}^{(i)})$  be the guesses for an initial condition on a (relative) periodic orbit and its period, which approximately satisfy (25). In order to bring them to a desired numerical precision, we utilize Newton's method as follows. Our goal is to find the small corrections  $(\Delta\hat{a}, \Delta T)$  which yield

$$\hat{a}_{\text{RPO}}^{(i)} + \Delta\hat{a} = \hat{f}^{T_{\text{RPO}}^{(i)} + \Delta T^{(i)}}(\hat{a}_{\text{RPO}}^{(i)} + \Delta\hat{a}). \quad (\text{A1})$$

Expanding (A1) to the linear order in  $\Delta\hat{a}$  and  $\Delta T$ , we obtain

$$\begin{aligned} \hat{a}_{\text{RPO}}^{(i)} + \Delta\hat{a} &\approx \hat{f}^{T_{\text{RPO}}^{(i)}}(\hat{a}_{\text{RPO}}^{(i)}) + \hat{J}^{T_{\text{RPO}}^{(i)}}(\hat{a}_{\text{RPO}}^{(i)})\Delta\hat{a} \\ &\quad + \hat{v}(\hat{f}^{T_{\text{RPO}}^{(i)}}(\hat{a}_{\text{RPO}}^{(i)}))\Delta T. \end{aligned} \quad (\text{A2})$$

Defining  $\hat{J}^{(i)} \equiv \hat{J}^{T_{\text{RPO}}^{(i)}}(\hat{a}_{\text{RPO}}^{(i)})$ ,  $\hat{v}^{(i)} \equiv \hat{v}(\hat{f}^{T_{\text{RPO}}^{(i)}}(\hat{a}_{\text{RPO}}^{(i)}))$ , and  $E^{(i)} = \hat{f}^{T_{\text{RPO}}^{(i)}}(\hat{a}_{\text{RPO}}^{(i)}) - \hat{a}_{\text{RPO}}^{(i)}$ , and rearranging the terms in (A2), we obtain the linear system of equations

$$(\mathbf{I} - \hat{J}^{(i)})\Delta\hat{a}^{(i)} - \hat{v}^{(i)}\Delta T^{(i)} = E^{(i)} \quad (\text{A3})$$

for the approximate corrections  $(\Delta\hat{a}^{(i)}, \Delta T^{(i)})$ . (A3) provides  $d$  equations for  $d + 1$  unknowns, where  $d$  is the dimension of the symmetry-reduced state space. We supplement (A3) with the constraint

$$\langle \hat{v}(\hat{a}_{\text{RPO}}^{(i)}), \Delta\hat{a}^{(i)} \rangle = 0, \quad (\text{A4})$$

which disallows for updating our guesses in the flow direction. We can now solve (A3) and (A4) for  $(\Delta\hat{a}^{(i)}, \Delta T^{(i)})$  and update our guesses as

$$\begin{aligned} \hat{a}_{\text{RPO}}^{i+1} &= \hat{a}_{\text{RPO}}^{(i)} + \alpha^k \Delta\hat{a}^{(i)}, \\ T_{\text{RPO}}^{i+1} &= T_{\text{RPO}}^{(i)} + \alpha^k \Delta T^{(i)}, \end{aligned} \quad (\text{A5})$$

where we introduced the step size  $\alpha^k \in (0, 1]$ . We set  $\alpha = 0.5$  and choose the smallest  $k = 0, 1, 2, \dots$  such that  $\|E_{i+1}\| <$

$\|E_i\|$ . We iterate this procedure until the error  $\|E_{i+1}\|$  is less than a tolerance  $\epsilon$ .

At each Newton step, we sample the relative periodic orbit with  $\lfloor T_{\text{RPO}}^i/\delta\tau \rfloor$  steps in time, hence the final converged time-step  $\delta\tau_{\text{RPO}}$  of the periodic orbit is close to the rest of the simulations.

## Appendix B: Edge-tracking algorithm

Let  $\langle L \rangle(\tau)$  denote the moving average of the angular momentum with a time-window  $\tau_w$  and  $\hat{a}_1$  and  $\hat{a}_2$  be two state vectors that belong to attractors  $\mathcal{M}_1$  and  $\mathcal{M}_2$ , respectively. We assume that  $\mathcal{M}_1$  and  $\mathcal{M}_2$  have mean angular momenta  $L_1$  and  $L_2$  respectively such that  $L_1 > L_{th,1}$  and  $L_2 < L_{th,2}$  for some thresholds  $L_{th,1}$  and  $L_{th,2}$ . We iterate the following algorithm in order to locate the edge that separates  $\mathcal{M}_1$  and  $\mathcal{M}_2$ 's basins of attraction.

```

while  $\|\hat{a}_1 - \hat{a}_2\| > \epsilon$  do
   $\hat{a}_3 \leftarrow (\hat{a}_0 + \hat{a}_1)/2$ 
  Set initial condition to  $\hat{a}_3$ 
  Compute  $\hat{a}(\tau)$  and  $\langle L \rangle(\tau)$  for  $\tau \in [0, \tau_f]$ 
  if  $\langle L \rangle(\tau_f) > L_1$  then
     $\hat{a}_1 \leftarrow \hat{a}_3$ 
  else if  $\langle L \rangle(\tau_f) < L_2$  then
     $\hat{a}_2 \leftarrow \hat{a}_3$ 
  else
    Terminate
  end if
end while

```

- <sup>1</sup>L. de Broglie. Ondes et quanta. *C. R.*, 177, 1923.
- <sup>2</sup>Y. Couder, E. Fort, C.-H. Gautier, and A. Boudaoud. From bouncing to floating: Noncoalescence of drops on a fluid bath. *Phys. Rev. Lett.*, 94(17):177801, 2005.
- <sup>3</sup>Y. Couder, S. Protière, E. Fort, and A. Boudaoud. Walking and orbiting droplets. *Nature*, 437(7056):208, 2005.
- <sup>4</sup>Y. Couder and E. Fort. Single-particle diffraction and interference at a macroscopic scale. *Phys. Rev. Lett.*, 97(15):154101, 2006.
- <sup>5</sup>A. Andersen, J. Madsen, C. Reichelt, S. Rosenlund Ahl, B. Lautrup, C. Ellegaard, M. T. Levinsen, and T. Bohr. Double-slit experiment with single wave-driven particles and its relation to quantum mechanics. *Phys. Rev. E*, 92:013006, 2015.
- <sup>6</sup>G. Pucci, D. M. Harris, L. M. Faria, and J. W. M. Bush. Walking droplets interacting with single and double slits. *J. Fluid Mech.*, 835:1136–1156, 2018.
- <sup>7</sup>J. W.M. Bush. Pilot-wave hydrodynamics. *Annu. Rev. Fluid Mech.*, 47(1):269–292, 2015.
- <sup>8</sup>E. Fort, A. Eddi, A. Boudaoud, J. Moukhtar, and Y. Couder. Path-memory induced quantization of classical orbits. *Proc. Natl. Acad. Sci.*, 107(41):17515–17520, 2010.
- <sup>9</sup>D. M. Harris and J. W. M. Bush. Droplets walking in a rotating frame: from quantized orbits to multimodal statistics. *J. Fluid Mech.*, 739:444–464, 2014.
- <sup>10</sup>S. Perrard, M. Labousse, M. Miskin, E. Fort, and Y. Couder. Self-organization into quantized eigenstates of a classical wave-driven particle. *Nature communications*, 5, 2014.
- <sup>11</sup>S. Perrard, M. Labousse, E. Fort, and Y. Couder. Chaos driven by interfering memory. *Phys. Rev. Lett.*, 113(10):104101, 2014.
- <sup>12</sup>A. U. Oza, R. R. Rosales, and J. W. M. Bush. A trajectory equation for walking droplets: hydrodynamic pilot-wave theory. *J. Fluid Mech.*, 737:552–570, 2013.
- <sup>13</sup>L. D. Tambasco, D. M. Harris, A. U. Oza, R. R. Rosales, and J. W. M. Bush. The onset of chaos in orbital pilot-wave dynamics. *Chaos: An Interdisciplinary Journal of Nonlinear Science*, 26(10):103107, 2016.
- <sup>14</sup>B. P. Luce. Homoclinic explosions in the complex Ginzburg-Landau equation. *Physica D*, 84:553–581, 1995.
- <sup>15</sup>P. Cvitanović, R. L. Davidchack, and E. Siminos. On the state space geometry of the Kuramoto-Sivashinsky flow in a periodic domain. *SIAM J. Appl. Dyn. Syst.*, 9:1–33, 2009.
- <sup>16</sup>N. B. Budanur and P. Cvitanović. Unstable manifolds of relative periodic orbits in the symmetry-reduced state space of the Kuramoto-Sivashinsky system. *J. Stat. Phys.*, 167(3):636–655, 2017.
- <sup>17</sup>A. P. Willis, P. Cvitanović, and M. Avila. Revealing the state space of turbulent pipe flow by symmetry reduction. *J. Fluid Mech.*, 721:514–540, 2013.
- <sup>18</sup>N. B. Budanur, K. Y. Short, M. Farazmand, A. P. Willis, and P. Cvitanović. Relative periodic orbits form the backbone of turbulent pipe flow. *J. Fluid Mech*, 833:274–301, 2017.
- <sup>19</sup>N. B. Budanur, P. Cvitanović, R. L. Davidchack, and E. Siminos. Reduction of the SO(2) symmetry for spatially extended dynamical systems. *Phys. Rev. Lett.*, 114:084102, 2015.
- <sup>20</sup>P. Chossat and R. Lauterbach. *Methods in Equivariant Bifurcations and Dynamical Systems*. World Scientific, Singapore, 2000.
- <sup>21</sup>M. Farazmand. An adjoint-based approach for finding invariant solutions of Navier-Stokes equations. *J. Fluid M.*, 795:278–312, 2016.
- <sup>22</sup>N. B. Budanur and B. Hof. Heteroclinic path to spatially localized chaos in pipe flow. *J. Fluid Mech*, 827, R1, 2017.
- <sup>23</sup>N. B. Budanur and B. Hof. Complexity of the laminar-turbulent boundary in pipe flow. *Phys. Rev. Fluids*, 3:054401, 2018.
- <sup>24</sup>P. Cvitanović, R. Artuso, R. Mainieri, G. Tanner, and G. Vattay. *Chaos: Classical and Quantum*. Niels Bohr Inst., Copenhagen, 2016.
- <sup>25</sup>C. W. Rowley and J. E. Marsden. Reconstruction equations and the Karhunen-Loève expansion for systems with symmetry. *Physica D*, 142:1–19, 2000.
- <sup>26</sup>J. Moláček and J. W. M. Bush. Drops bouncing on a vibrating bath. *J. Fluid Mech.*, 727:582–611, 2013.
- <sup>27</sup>M. Labousse, A. U. Oza, S. Perrard, and J. W. M. Bush. Pilot-wave dynamics in a harmonic potential: Quantization and stability of circular orbits. *Phys. Rev. E*, 93:033122, Mar 2016.
- <sup>28</sup>K. M. Kurianski, A. U. Oza, and J. W. M. Bush. Simulations of pilot-wave dynamics in a simple harmonic potential. *Phys. Rev. Fluids*, 2:113602, Nov 2017.
- <sup>29</sup>Matthieu Labousse. *Etude d'une dynamique à mémoire de chemin: une expérimentation théorique*. PhD thesis, Université Paris 6, 2014.
- <sup>30</sup>S. Perrard and M. Labousse. Transition to chaos in wave memory dynamics in a harmonic well: Deterministic and noise-driven behavior. *Chaos: An Interdisciplinary Journal of Nonlinear Science*, 28(9):096109, 2018.
- <sup>31</sup>G. N. Watson. *A Treatise on the Theory of Bessel Functions*. Cambridge University Press, 1944.
- <sup>32</sup>E. Jones, T. Oliphant, P. Peterson, et al. SciPy: Open source scientific tools for Python, 2001.
- <sup>33</sup>Y. Kuznetsov. *Elements of Applied Bifurcation Theory*. Applied Mathematical Sciences. Springer New York, 2010.
- <sup>34</sup>E. Doedel, H. B. Keller, and J. P. Kernevez. Numerical analysis and control of bifurcation problems (i): Bifurcation in finite dimensions. *Int. J. Bifurcat. Chaos*, 01(03):493–520, 1991.
- <sup>35</sup>J. W. Swift and K. Wiesenfeld. Suppression of period doubling in symmetric systems. *Phys. Rev. Lett.*, 52:705–708, 1984.
- <sup>36</sup>C. Grebogi, E. Ott, and J. A. Yorke. Chaotic attractors in crisis. *Phys. Rev. Lett.*, 48:1507–1510, May 1982.
- <sup>37</sup>C. Grebogi, E. Ott, and J. A. Yorke. Crises, sudden changes in chaotic attractors, and transient chaos. *Physica D*, 7(1):181–200, 1983.
- <sup>38</sup>K. T. Alligood, T. D. Sauer, and J. A. Yorke. *Stable Manifolds and Crises*, pages 399–445. Springer Berlin Heidelberg, Berlin, Heidelberg, 1997.
- <sup>39</sup>T. Itano and S. Toh. The dynamics of bursting process in wall turbulence. *J. Phys. Soc. Japan*, 70:701–714, 2001.
- <sup>40</sup>S. Toh and T. Itano. A periodic-like solution in channel flow. *J.*



- Fluid Mech.*, 481:67–76, 2003.
- <sup>41</sup>T. M. Schneider, B. Eckhardt, and J. Yorke. Turbulence, transition, and the edge of chaos in pipe flow. *Phys. Rev. Lett.*, 99:034502, 2007.
- <sup>42</sup>T. M. Schneider, J. F. Gibson, M. Lagha, F. De Lillo, and B. Eckhardt. Laminar-turbulent boundary in plane Couette flow. *Phys. Rev. E.*, 78:037301, 2008.
- <sup>43</sup>F. Mellibovsky, A. Meseguer, T. M. Schneider, and B. Eckhardt. Transition in localized pipe flow turbulence. *Phys. Rev. Lett.*, 103:054502, Jul 2009.
- <sup>44</sup>T. M. Schneider, D. Marinc, and B. Eckhardt. Localized edge states nucleate turbulence in extended plane Couette cells. *J. Fluid Mech.*, 646:441–451, 2010.
- <sup>45</sup>S. Zammert and B. Eckhardt. A spotlike edge state in plane Poiseuille flow. *PAMM*, 14:591–592, 2014.
- <sup>46</sup>T. Khapko, T. Kreilos, P. Schlatter, Y. Duguet, B. Eckhardt, and D. S. Henningson. Edge states as mediators of bypass transition in boundary-layer flows. *J. Fluid Mech.*, 801, 2016.
- <sup>47</sup>P. Chossat and M. Golubitsky. Symmetry-increasing bifurcation of chaotic attractors. *Physica D*, 32(3):423 – 436, 1988.
- <sup>48</sup>S. E. Newhouse, D. Ruelle, and F. Takens. Occurrence of strange Axiom A attractors near quasi-periodic flows on  $T^m$  ( $m = 3$  or more). *Commun. Math. Phys.*, 64:35, 1978.
- <sup>49</sup>S. H. Strogatz. *Nonlinear Dynamics and Chaos*. Perseus Books, Cambridge, MA, 2000.
- <sup>50</sup>E. N. Lorenz. Deterministic nonperiodic flow. *J. Atmos. Sci.*, 20:130–141, 1963.
- <sup>51</sup>P. Cvitanović. Periodic orbit theory in classical and quantum mechanics. *Chaos*, 2(1):1–4, 1992.
- <sup>52</sup>M. Durey and P. A. Milewski. Faraday wave-droplet dynamics: discrete-time analysis. *J. Fluid Mech.*, 821:296–329, 2017.
- <sup>53</sup>A. U. Oza, Ø. Wind-Willassen, D. M. Harris, R. R. Rosales, and J. W. M. Bush. Pilot-wave hydrodynamics in a rotating frame: Exotic orbits. *Phys. Fluids*, 26(8):082101, 2014.